# Biodegradable zinc-based materials with a polymer coating designed for biomedical applications

## Citation

ORIŇÁKOVÁ, Renáta, Radka GOREJOVÁ, Viktória ČÁKYOVÁ, Miroslav DŽUPON, Miriam KUPKOVÁ, Tibor SOPČÁK, Kadir ÖZALTIN, Matej MIČUŠÍK, Ondrej PETRUŠ, Mária OMASTOVÁ, Marek VOJTKO, and Petr SÁHA. Biodegradable zinc-based materials with a polymer coating designed for biomedical applications. *Journal of Applied Polymer Science* [online]. John Wiley and Sons Inc, 2023, [cit. 2025-04-25]. ISSN 0021-8995. Available at https://onlinelibrary.wiley.com/doi/10.1002/app.54773

## DOI

https://doi.org/10.1002/app.54773

## Permanent link

https://publikace.k.utb.cz/handle/10563/1011736

---

# Biodegradable zinc-based materials with a polymer coating designed for biomedical applications

**Renáta Oriňaková[1,2], Radka Gorejová[1,2], Viktória Čákyová[1], Miroslav Džupon[3], Miriam Kupková[3], Tibor Sopčák[3], Kadir Özaltin[2], Matej Mičušík[4], Ondrej Petruš[3], Mária Omastová[4], Marek Vojtko[3], Petr Sáha[2]**

*[1]Department of Physical Chemistry, Faculty of Science, Pavol Jozef Safárik University in KoSice, KoSice, Slovakia*

*[2]Centre of Polymer Systems, University Institute, Tomas Bata University in Zlín, Zlín, Czech Republic*

*[3]Slovak Academy of Sciences, Institute of Materials Research, KoSice, Slovakia*

*[4]Slovak Academy of Sciences, Polymer Institute, Bratislava, Slovakia*

*Correspondence: Radka Gorejová, Department of Physical Chemistry, Faculty of Science, Pavol Jozef Safarik University in Košice, Moyzesova 11, Košice 041 54, Slovakia. Email:* ***radka.gorejova@upjs.sk, gorejova@utb.cz***

## Abstract

Over the last decades, biodegradable metals have gained popularity for biomedical applications due to their ability to assist in tissue healing. These materials degrade in vivo, while the corrosion products formed are either absorbed or excreted by the body, and no further surgical intervention is required for removal. Intensive research has been carried out mainly on degradable biomaterials based on Mg and Fe. In recent years, zinc-based degradable biomaterials have been explored by the biomedical community for their intrinsic physiological relevance, desirable biocompatibility, intermediate degradation rate, tuneable mechanical properties and pro-regeneration properties. Since pure Zn does not exhibit sufficient mechanical properties for orthopedic applications, various Zn alloys with better properties are being developed. In this work, the combined effect of minor Fe addition to Zn and a polyethyleneglycol ($PEG$) coating on the surface morphology, degradation, cytotoxicity and mechanical properties of Zn-based materials was studied. There are several studies regarding the influence of the production of Zn alloys, but the effect of polymer coating on the properties of Zn-based materials has not been reported yet. A positive effect of Fe addition and polymer coating on the degradation rate and mechanical properties was observed. However, a reduction in biocompatibility was also detected.

**KEYWORDS**: Biocorrosion, iron, polyethylene glycol coating, zinc, zinc-iron alloy

# 1 INTRODUCTION

Based on statistical data, about 20 million people worldwide suffer from damaged or lost bone tissue each year.[1,2] This can occur for a variety of reasons, for example, traumatic injury, diseased bone, and an increasing number of accidents.[3] In addition, the extension of the average life expectancy of modern humans has led to an increased incidence of skeletal ailments and diseases in the elderly (e.g., rheumatoid arthritis, osteoporosis, bone fractures, and bone cancer),[5] with other related health concerns.[3-6] This usually leads to a deterioration in the quality of life and can even make patients immobile.[3] There is currently no gold standard for repairing bone defects in the supporting parts of the skeleton.[4]

Over the past decades, advances in medical technology and innovations in biomaterials have enabled the rapid development of high-performance implantable biomaterials that can improve patients' lives by replacing and repairing soft and hard tissues in traumatology, vascular therapy, orthopedics, dentistry and wound healing.[1,3,5,7,8] Typical materials currently used in orthopedic applications include metals, polymers and bioceramics.[4,9] However, polymeric and bioceramic materials do not provide the necessary mechanical support for damaged bones in weight-bearing applications.[4,7,9] Moreover, metals can be easily handled by common methods, such as powder metallurgy, machining, forming and casting.[4,7,9,10] On the other hand, metallic materials exhibit suitable mechanical properties but are not osteogenically active.

Non-degradable metallic biomaterials, such as cobalt-chromium alloys ($Co-Cr-Mo$), titanium alloys ($Ti, Ti-Al-V, Ti-Al-Nb$), super elastic $Ni-Ti$ and stainless steels ($SS$), are currently used primarily for permanent implants to maintain load-bearing hard tissue function by providing mechanical support.[3,7-13] These metallic materials possess a high corrosion resistance to human-body fluids. However, due to their permanent presence in the body, long-term clinical complications may occur, including pain, allergic reactions, chronic inflammation, migration of the implant and thrombus formation.[4,7-9,11,12] Furthermore, the difference between the modulus of elasticity of these metallic materials and the modulus of elasticity of natural human bone causes stress shielding or bone mass loss. The above-mentioned problems related to permanent biomedical implants may impair the therapeutic effect of the implant, which often requires reintervention to replace or remove it.[3,7,8,10,12,13]

In addition, for many applications only a temporary implant is required and is no longer necessary after complete recovery of the damaged tissue. Consequently, there is a great effort to replace the existing non-degradable implant devices with transient functionality with biodegradable alternatives. Thus, subsequent surgical removal is no longer required, which considerably reduces the medical cost, morbidity and additional inconvenience to the patient.[7-12,14]

Bioabsorbable or biodegradable metals, as they are referred to, are a novel class of bio-active structural materials that have been extensively studied in the last decades mainly for orthopedic and vascular applications.[3,9,13,15-17]

A biodegradable implant gradually and harmlessly degrades in the body environment during the remodeling period of the diseased bone while still maintaining mechanical integrity and is progressively replaced by new bone tissue. Upon fulfilling their support function, biodegradable materials dissolve entirely, whereby the corrosion products are bio-safe to human health, not toxic, carcinogenic or allergenic, and can be absorbed or metabolized by the body.[1,7-11,13,15,18]

To date, magnesium, iron, zinc and their alloys have been extensively researched as potential biodegradable metals for hard tissue applications.[3,7-9,11-13,15,16,18-20]

Biodegradable implants based on Mg are particularly interesting because of their exceptional biocompatibility, ability to promote bone cell activation, and bone-mimicking elastic modulus significantly eliminating the stress-shielding effect. However, Mg and its alloys exhibit a rapid corrosion rate under the physiological conditions associated with hydrogen gas evolution, resulting in pH increase and an early loss of mechanical integrity.[9,11-13,16,19-21]

Bioabsorbable Fe-based materials are attractive for orthopedic implants mainly due to their good biocompatibility, outstanding mechanical properties and excellent formability. Iron is also a vital nutrient and an essential trace element in the human body.[3,8,15,19] However, $Fe$ and $Fe$-based alloys degrade very slowly, and these materials, as well as their corrosion products, are retained in tissues for long periods, producing complications analogous to those found with permanent implants.[7,11-13,16,22]

The shortcomings associated with Mg- and $Fe$-based systems have stimulated research into new metallic biomaterials, including $Zn$ and $Zn$-based alloys. Recently, $Zn$-based metals have been considered promising biodegradable and biocompatible materials for biomedical applications, particularly temporary orthopedic bone implants, fixation devices, wound closure devices and cardiovascular stents.[16,20,22,23]

Biodegradable zinc-based materials are widely researched thanks to their superior mechanical properties, good biocompatibility, adaptability, moderate in vivo degradation rate, positive effect on the human body and the significant functional biological and physiological roles of Zn.[3,4,8,10,11,15,21,24-26]

Zinc is a nutritionally essential biogenic element required for the maintenance of physiological functions of the human body. It supports the immune and nervous systems, bone mineralization, bone formation, wound healing, cell proliferation and division, promotes collagen synthesis and has osteogenic and antibacterial properties.[7-11,18,21,23,24,26] In addition, zinc plays a crucial role in gene expression and maintaining structural integrity; it serves as a cofactor in all types of enzymes and participates in nucleic acid metabolism, protein regulation and brain development.[14-16,20,23-25] Another advantage of zinc is that it does not normally accumulate in the body and is excreted in the feces and urine.[17,27]

Moreover, alongside the degradation rate of $Zn$ materials between those of Mg and $Fe$, their degradation products are fully bioresorbable without unwanted excessive release of hydrogen. Due to a low melting point (420° C) of zinc, low chemical reactivity in the molten state and good machinability, its processing and fabrication in air without requiring a special environment is possible [3,7,10,11,13,15-17,20,21,26] As a result, Zn and its alloys are a highly studied research topic in the field of biodegradable metallic materials.

Nevertheless, an important limitation of pure zinc is its poor mechanical properties, such as brittleness, softness, low mechanical strength, creep resistance and plasticity. To meet the requirements for load-bearing orthopedic applications, it is desirable to alloy it with the other elements. The most frequently studied alloying elements are magnesium (Mg), aluminium ($Al$), copper ($Cu$), calcium ($Ca$), manganese ($Mn$), silver ($Ag$), strontium ($Sr$), lithium ($Li$) and germanium ($Ge$). Alloying elements and techniques also determine the degradation mode of $Zn$-based alloys. The above traits of zinc alloys make them suitable as a candidate biodegradable material for biomedical applications.[8,18,20,21,26]

The growing interest in biodegradable materials for temporary orthopedic implants is focused on the research of biomaterials with a desirable degradation rate, biocompatibility and mechanical properties the same as those of natural bone. The rate of degradation of short-term implant devices must be consistent with the rate of remodeling of the damaged bone and must also correspond to the clinical application. However, the most important challenge concerns controlling the concentration of degradation products released in order to avoid their accumulation and toxic levels of metal concentrations. The biodegradation rates for $Mg$-based materials, $Zn$-based materials and $Fe$-based materials in the physiological environment are in the range <0.23, 0.02-0.10 and 0.001-0.090 mm year$^{-1}$, respectively.[28] According to recent studies, the biodegradation rate of zinc biomaterials is insufficient for most biomedical applications.[3] Functional polymer coatings and modifying the composition of biomaterials by alloying elements can alter the degradation rate and improve the mechanical properties of pure $Zn$.[16,25,29,30] Together with $Cu$ and $Mn$, $Fe$ belongs among the so-called crucial elements in the human body, which positively affect bone health and metab-olism.[8] In addition, $Fe$ can enhance the mechanical properties of $Zn$-based materials. The improvement of mechanical properties, biocompatibility and hemocompatibility and an increase in the corrosion rate of $Fe$ materials due to a polyethylene glycol ($PEG$) coating was reported in our previous papers.[29-32] However, $Zn$-based biomaterials with a polymer coating layer have not been studied thus far. In this work, the effect of a polymer coating on the properties of Zn-based biomaterials was evaluated for the first time. The study of the corrosion behavior, mechanical properties and hemocompatibility of biodegradable zinc-iron alloys was performed in our previous papers,[17,33] in which $Zn - Fe$ alloys that contained 5 and more wt. % of iron was found to show worse mechanical properties and lower hemocompatibility than alloys with lower Fe content. In this study, the simultaneous effect of both the addition of a low concentration of Fe (1 and 2 wt. %) to $Zn$ and coating with a $PEG$ layer on the surface appearance, microstructure, in vitro degradation behavior, cytotoxicity and mechanical properties of $Zn$-based materials was evaluated.

## 2 MATERIALS AND METHODS

### *2.1 Metallic samples and PEG coating preparation*

The zinc-based materials were prepared from zinc powder (99.9% purity, Centralchem, Slovakia) and iron powder (99.5% purity, Alfa Aesar, Germany). Samples from pure zinc ($Zn$), zinc with 1 wt. % of iron ($Zn - 1Fe$) and zinc with 2 wt. % of iron ($Zn - 2Fe$) were used for the study. Raw zinc and iron powders were manually mixed for 10 min before sample preparation. Pellets with a diameter of 12 mm and height of ~4 mm were prepared by uniaxial compression at 600 MPa using a hydraulic press (Redats H-380, P.H.U Szczepan, Krakow, Poland). Green compacts were heated from laboratory temperature to 350° C with a heating rate of 5°C.min$^{-1}$ in an argon atmosphere (flow rate 4 L.min$^{-1}$) using a ceramic furnace (Nabertherm 303000, Nabertherm GmbH, Germany). The temperature was held at 350°C for 60 min and the samples were left to cool to laboratory temperature.

After sintering, samples were ground with two different grids (240 and 800 grids) and ultrasonically cleaned in acetone and ethanol, in each for 10 min, before application of the polyethyleneglycol ($PEG$, $M_r = 4000$, Merck KGaA, Germany) coating. Crystalline $PEG$ was dissolved in 96 vol. % ethanol (Centralchem, Slovakia) to obtain a 10 wt. % concentration of the dip-coating solution. Subsequently, the ground and cleaned samples were immersed in the $PEG$ solution for 90 min and then dried at 45° C for 3 h.

### *2.2 Material characterization*

The surface morphology of uncoated and $PEG$-coated samples was observed using a digital microscope (Dino-Lite Edge Model AM4815ZT ($20x$ $-220x$, EDOF+EDR) and Dino-Lite Edge Model AM4515T8, Dino-Lite, Dino-Lite Europe, Netherlands).

Scanning electron microscopy ($SEM$) coupled with energy-dispersive spectrometry ($EDX$) (JEOL JSM-7000F, with EDX INCA, Japan, and ZEISS AURIGA COMPACT, Germany) was chosen for further surface morphology examination before and after corrosion.

The samples' microstructure was analyzed using both a light microscope (Olympus GX71, Japan) and a scanning electron microscope (EVO MA15 EDX/WDX from Oxford Instruments, Abingdon, United Kingdom). Prior to metallographic examination, selected samples were mounted, ground and polished with a 0.1 mm diamond paste. The microstructure was revealed through etching in a 0.5 percent aqueous NaOH solution.

Raman spectra for surface examination were recorded by an XploRA ONE Raman microscope (Horiba Jobin Yvon) with a 532 nm laser and magnification objective -10 × in the range of 200-1800 $cm^{-1}$.

The phase composition of the $Zn$ and $Zn-Fe$ samples and the $PEG$ coating was studied by $X$-ray diffraction ($XRD$) using a Philips $X$'Pert Pro $X$-ray diffractometer (Cu K$\alpha$ radiation, 40 kV, 50 mA, $2\theta$ between 10 and 90.

Surface topology characteristics on the samples were obtained with an atomic force microscope ($AFM$) using a Dimension Icon (Bruker, Karlsruhe, Germany). All experiments were performed by peak force tapping mode using a ScanAsyst-Air Si/Ňitride probe (Bruker, Santa Barbara, CA, USA) with $k =$ 0.4 N/m of spring constant value of the cantilever. A scanning area of 1 × 1 $\mu$m for each sample was investigated with a frequency of 1 Hz. Average surface roughness ($Ra$) values were analyzed using NanoScope Analysis software.

$XPS$ signals were recorded using a Thermo Scientific NEXSA-G2 $XPS$ system (Thermo Fisher Scientific, UK) equipped with a micro-focused, monochromatic Al K$\alpha$ $X$-ray source (1486.68 eV). An $X$-ray beam of 400 mm size was used. The spectra were acquired in the constant analyzer energy mode with a pass energy of 200 eV for the survey. Narrow regions were collected with a pass energy of 50 eV, with an energy step size of 0.1 eV. Charge compensation was achieved using a flood gun system. The Thermo Scientific Advantage software, version 6.5.0 (Thermo Fisher Scientific), was used for digital acquisition and data processing. Spectral calibration was determined using the automated calibration routine and the internal $Au$, $Ag$ and $Cu$ standards supplied with the NEXSA-G2 system. The surface compositions (in atomic %) were determined by considering the integrated peak areas of the detected atoms and the respective Scofield sensitivity factors.

### *2.3 Electrochemical corrosion testing*

The potentiodynamic polarization method was used to evaluate the degradation behavior of the studied samples using a Multichannel Autolab M204 potentiostat (Metrohm, Switzerland). Uncoated samples were ultra-sonically cleaned in acetone and ethanol for 10 min each before measurements, and all samples were examined in triplicate ($n = 3$). A three-electrode system with Pt as the counter electrode, Ag/AgCl/KCl (3 $mol.L^{-1}$) as the reference electrode and metallic samples as the working electrodes were used. The open circuit potential ($OCP$) was determined and stabilized before each measurement for 60 min. Corrosion measurements were performed under static conditions in a double-wall electrochemical cell tempered by an external circulation thermostat to 37°C with 0.1 mV $s^{-1}$ scan rate. A Hanks' solution with the following composition (in $g.L^{-1}$): 8 NaCl, 0.4 KCl, 0.14 $CaCl_2$, 0.06 $MgSO_4.7H_2O$, 0.06 $NaH_2PO_4.2H_2O$, 0.35 $NaHCO_3$, 1.00 glucose, 0.60 $KH_2PO_4$ and 0.10 $MgCl_2.6H_2O$ - was used as the corrosive medium. Corrosion rates were calculated from the equation:

$$CR = \frac{j_{corr} \cdot EW \cdot K}{\rho} \qquad (1)$$

where $CR$ is the corrosion rate (mm year$^{-1}$), $j_{corr}$ stands for corrosion current density ($\mu$A cm$^{-2}$), $EW$ is the equivalent weight, $\rho$ is the sample density (cm$^3$) and $K$ is a constant ($3.27 \times 10^{-3}$) determining the output units of the $CR$. Due to the low content of both $Fe$ and $PEG$, $EW$ of bare $Zn$ (32.69 g/eq) was used to calculate the $CR$ for all samples.

### *2.4 Immersion corrosion testing*

Uncoated samples were ultrasonically cleaned in acetone and ethanol for 10 min each and oven-dried at 55°C. A total of 50 mL (based on the sample surface area) of Hanks' solution as a corrosive medium with uniform access to the whole sample surface was used. Samples were held at 37° C for 4 weeks. Afterward, they were removed from the testing solution, rinsed with distilled water and ultrasonically cleaned in ethanol for 10 min. After 4 weeks, the pH of the medium was measured, and the surface morphology of the corroded samples was studied. The corrosion rate ($CR$ in mm year$^{-1}$) was calculated from the mass changes using Equation (**2**) based on the ASTM G31 standard[**34**]:

$$CR = \frac{8.76 \times 10^4 \left(m_i - m_f\right)}{\rho A t} \qquad (2)$$

where $m_i$ and $m_f$ are the initial mass (g) and the final mass after corrosion (g), A is the exposed surface area of the sample (cm$^2$), $\rho$ is the density of metallic sample (g/cm$^3$) and t is the immersion time ($h$). Before the determination of the final mass, the samples were subjected to chemical cleaning in a solution consisting of 100 g L$^{-1}$ NH4Cl for 2-5 min at 70° C to remove corrosion products according to ISO 8407.[**35**]

### *2.5 Cytotoxicity evaluation*

#### *2.5.1 Extracts preparation*

UV-disinfected samples ($PEG$-coated and uncoated $Zn$, $Zn - 1Fe$, $Zn - 2Fe$ and a stainless-steel sheet as a control) were placed into sterile polypropylene centrifuge tubes, and 2 mL of the complete culture medium (Dulbecco's Modified Eagle's Medium with 10% fetal bovine serum ($FBS$) and 1% antibiotic solution) was added into each tube, and the samples were incubated at 37° C for 24 h. After 24 h of incubation, all samples were gently removed and the medium was centrifuged (10,000 rpm, 10 min) to collect the remedies-free extracts. The supernatants (extracts) were used for cytotoxicity testing. Extracts were further diluted to 100%, 50% and 10% with a complete culture medium to study the dependence of cell viability on extract concentration.

### *<u>2.5.2 MTS test</u>*

The cytotoxicity evaluation was performed according to the STN ISO 10993-5 standard.[36] The $1 \times 10^4$ adult human dermal fibroblast ($HDFa$) cells obtained from Sigma Aldrich were suspended in 100 mL of complete culture medium and seeded into a 96-well cell microplate. The cells were incubated at 37°C in 95% humidity and 5% $CO_2$ for 24 h to culture semi-confluent monolayers of $HDFa$ cells. The culture medium from each well was removed after 24 h of incubation and the wells were rinsed with phosphate-buffered saline ($PBS$). Subsequently, 100 qL of 100%, 50% and 10% extracts were added to the wells with seeded cells and were left to incubate for 4 or 24 h, and 100 qL of fresh complete culture medium was used as a negative control. All experiments were carried out in triplicate ($n = 3$). Cytotoxicity was evaluated using the $MTS$ proliferation test assay (Cell titer 96 aqueous one solution cell proliferation assay, Promega, USA). The absorbance of formazan produced by the mitochondrial enzyme activity after 4/24 h of cultivation was measured, and relative cell viability was evaluated.

### *2.6 Mechanical properties testing*

Cylindrical specimens with a diameter of approximately 12 mm and a height of around 2 mm were utilized for the compression tests. A TiraTest 2300 universal testing machine from Germany was employed to conduct the measurements, with a ram speed of 0.2 mm/min. The compressive 0.2% proof stress was determined by evaluating the stress at 0.2% plastic strain. The compres�sion testwas stopped at a stress of 680 MPa.

## **3 RESULTS AND DISCUSSION**

### *3.1 Surface morphology and microstructure*

### *<u>3.1.1 Uncoated samples</u>*

The $Zn$ and $Zn - Fe$ materials were produced from the same $Zn$ and $Fe$ powders and by the same method as in our previous study,[17] but in this study, the raw zinc and iron powders were mixed manually for 10 min before sample preparation instead of mixing in a laboratory mixer for 1 h. The particles of both powdered metals were spherical in shape. The size of zinc and iron powder particles was in the range from 1 to 10 $\mu$m and from 0.15 to 14.5 $\mu$m, respectively. Figure 1 shows the surface morphology (optical images **Figure 1a-c**, SEM micrographs **Figure 1d-f**) of the individual metallic samples in the air together with $AFM$ images of the surface, and the average surface roughness values obtained from $AFM$ analysis. From the optical micrographs (**Figure 1a-c**), no differences in the surface appearance can be observed. The surface of all the samples is even, continuous and smooth, with clear grooves after the grinding. The surface morphology of all the prepared materials is similar, although a decrease in homogeneity with increasing $Fe$ content can be observed from the $SEM$ images (**Figure 1d-f**). In addition, the granular structure of the surface, which is the result of the metal pellet preparation method consisting of pressing and sintering powder particles, can be seen from the $SEM$ micrographs as well as from the $AFM$ images (**Figure 1g-i**). The average surface roughness values for all the samples are very close, between 6.05 and 6.78 nm.

The microstructure of sintered $Zn$ and $Zn - Fe$ samples was observed using an $SEM$ and optical metallo-graphic microscope on polished and etched crosssections, and the element composition was analyzed by $EDX$.

**Figures 2a,b** show micrographs of a cross section of sintered zinc samples, which illustrate the microstructure of these samples. The microstructure consists of nonhomogeneously distributed globular zinc particles with sizes ranging from 1 to 10 $\mu$m. Elemental analysis revealed the presence of only $Zn$ and $O$ (see **Figure 1b**, **Table S1**, area analysis). Inside the globular zinc particles, the concentration of oxygen was up to 2.7 at. % (**Figure 2b**, **Table S1**, Points 2, 3). A locally increased oxygen concentration was detected at the boundaries of the zinc particles (**Figure 1b**, Table S1, **Point 4**; **Figure 1c-e**).

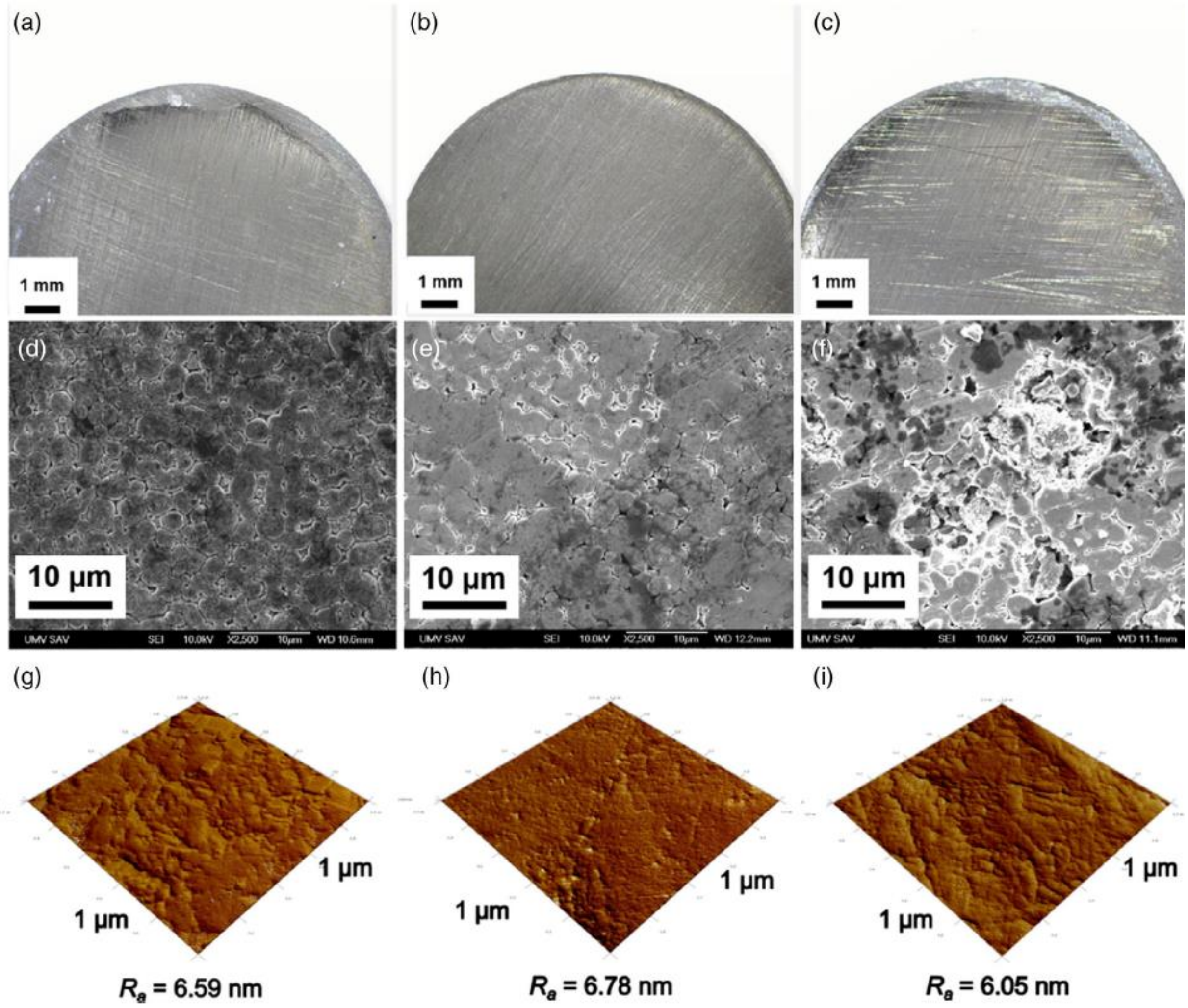

**FIGURE 1** Optical images of the surface of $Zn$ (a), $Zn - 1Fe$ (b) and $Zn - 2Fe$ (c) pellets before coating, and corresponding $SEM$ images of the surface of $Zn$ (d), $Zn - 1Fe$ (e) and $Zn - 2Fe$ (f); $AFM$ images of the surface and average surface roughness ($R_a$) values for $Zn$ (g), $Zn - 1Fe$ (h) and $Zn - 2Fe$ (i). [Color figure can be viewed at **wileyonlinelibrary.com**]

The $Zn - 1Fe$ samples exhibited a microstructure characterized by non-uniformly sized zinc grains (originated from zinc powder particles), which were mainly globular in shape, and massive $Fe$-based grains (originated from iron powder particles) without sharp edges. The size of the zinc grains varied from 1 to 10 $\mu$m. Fe-based grains were predominantly spheroidal and irregular in shape, up to 20 $\mu$m in size (as shown in **Figure 3a,b**). The matrix of the $Zn - 1Fe$ samples contained zinc, iron and oxygen, while the concentration of zinc in the massive $Fe$ grains was found to be up to 2.6 at. %, (**Figure 3b, Table S2**). Both line and area $EDX$ analysis showed low concentrations of zinc in the iron grains, as demonstrated in **Figure 3c-e** (line analysis) and **Figure 3f,g** (area analysis).

The microstructure of the $Zn - 2Fe$ samples (**Figure 4a,b**). was the same as the microstructure of the $Zn - 1Fe$ samples (**Figure 3a,b**). The Zn-2Fe samples also contained zinc, iron and oxygen, as shown in **Figure 4b** and **Table S3**. In this sample, massive iron grains contained up to 4.4 at. % of zinc, as indicated in **Figure 4b**, **Table S3**, Point 2 and Point 3. Both line and area $EDX$ analysis confirmed the presence of zinc in iron grains, as demonstrated in **Figure 4c-e** (line analysis) and **Figure 4f,g** (area analysis).

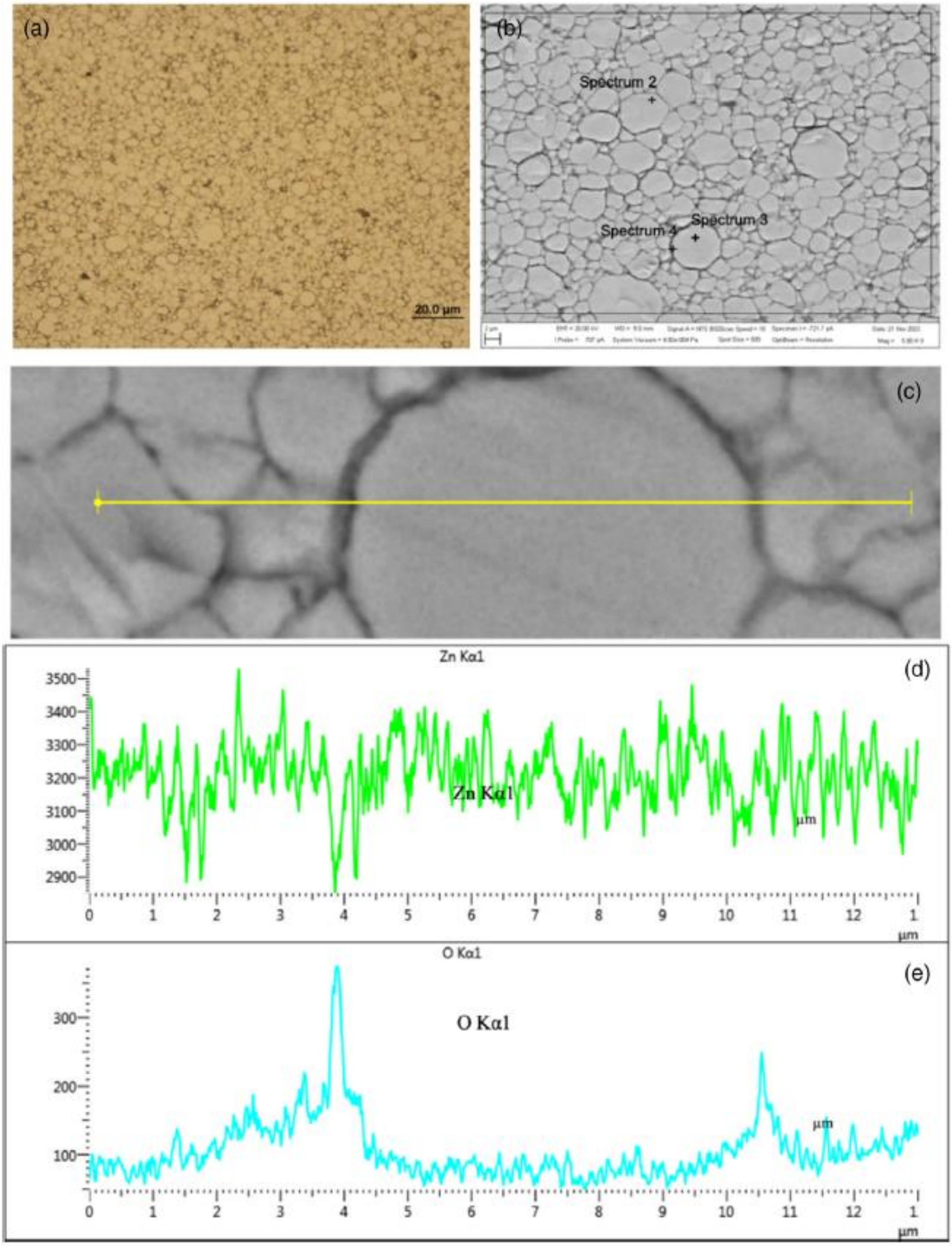

**FIGURE 3** Micrographs and $EDX$ microanalysis of polished and etched sections through the interior of sintered $Zn-1Fe$ sample; (a) light microscopy; (b) $SEM$ with the area and points of $EDX$ elemental analysis; (c) $SEM$ with the detail of the microstructure and the line of $EDX$ elemental microanalysis; (d) the distribution of $Zn$ from line $EDX$ analysis; (e) the distribution of $Fe$ from line $EDX$ analysis; (f) the distribution of $Zn$ from area $EDX$ analysis; (g) the distribution of Fe from area $EDX$ analysis; (h) $SEM$ with the detail of microstructure and the area of $EDX$ elemental microanalysis. [Color figure can be viewed at **wileyonlinelibrary.com**]

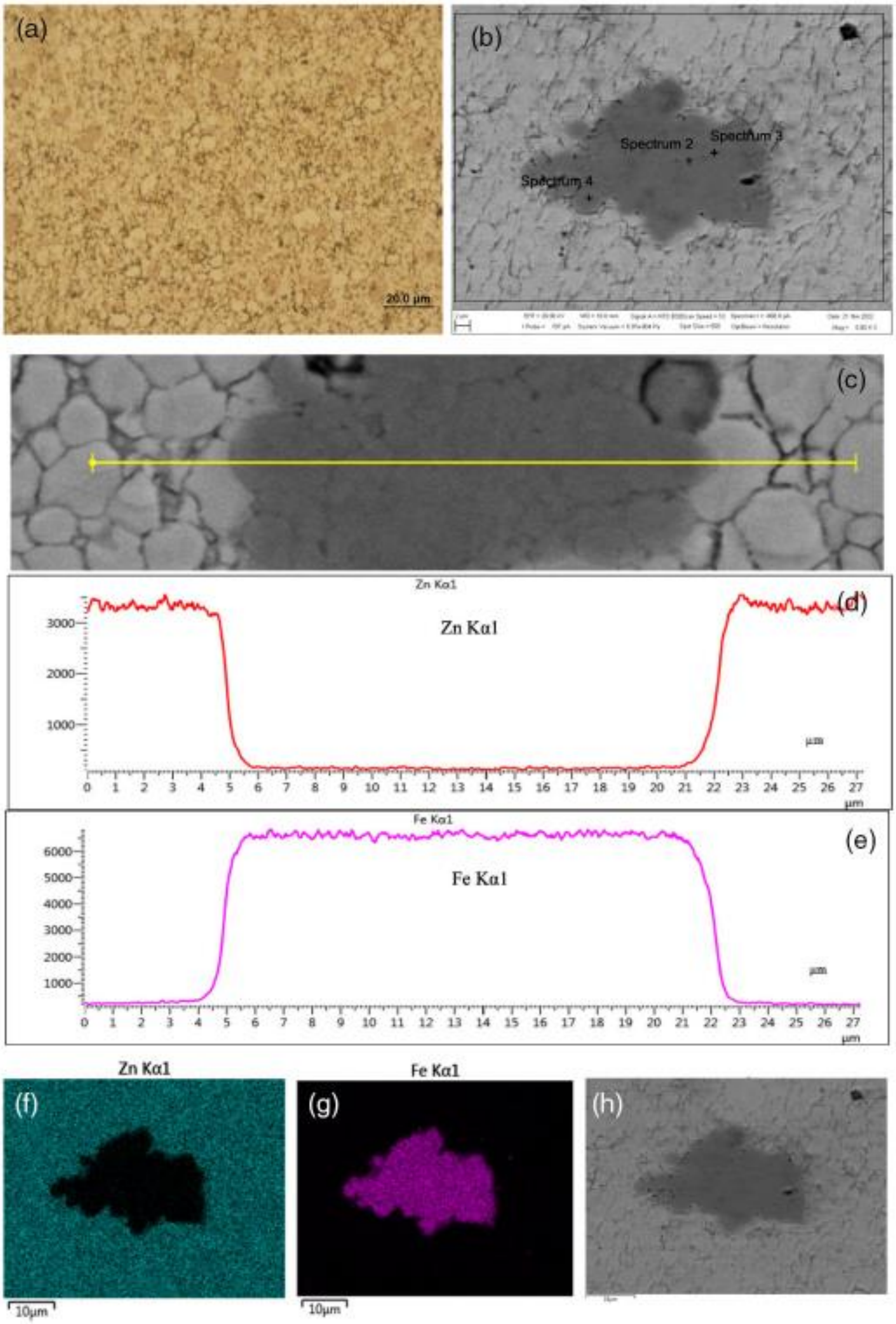

**FIGURE 3** Micrographs and $EDX$ microanalysis of polished and etched sections through the interior of sintered $Zn - 1Fe$ sample; (a) light microscopy; (b) $SEM$ with the area and points of $EDX$ elemental analysis; (c) $SEM$ with the detail of the microstructure and the line of $EDX$ elemental microanalysis; (d) the distribution of Zn from line $EDX$ analysis; (e) the distribution of Fe from line $EDX$ analysis; (f) the distribution of Zn from area $EDX$ analysis; (g) the distribution of $Fe$ from area $EDX$ analysis; (h) $SEM$ with the detail of microstructure and the area of $EDX$ elemental microanalysis. [Color figure can be viewed at **wileyonlinelibrary.com**]

### *3.1.2 PEG coated samples*

$SEM$ micrographs together with $AFM$ images and the average surface roughness values for metallic samples with a $PEG$ layer are depicted in **Figure 5a-i**. As shown in Figure 5a-c, after the deposition of the polymer layer, the granular structure and grooves were covered with a coherent layer of polymer and the surface was smoother compared to uncoated samples. This is consistent with the average surface roughness values, which are half as low compared to the values for uncoated samples (in the range from 3.14 to 3.77 nm) and confirm a decrease in the surface roughness. The wavy surface topography of the polymer layer is clearly visible in the $SEM$ images at higher magnification (**Figure 5d-f**) and in the $AFM$ images (**Figure 5g—i**). The amount of polymer deposited on the surface of the metal samples, determined from the difference in weight of samples before and after the deposition of the coating, was in the range of 0.280.43 wt.%. The thickness of the polymer layer determined from the micrographs of a cross section of the $PEG$-coated samples was in the range from 5 to 9 $\mu$m.

The formation of intermetallic phases in the Zn-Fe samples was investigated by means of $XRD$ analysis. **Figure 5j** shows the $XRD$ spectrum of uncoated metallic samples ($Zn, Zn-1Fe$ and $Zn-2Fe$), $PEG$-coated samples ($Zn + PEG$, $Zn-1Fe + PEG$ and $Zn-2Fe + PEG$) and crystalline pure $PEG$. The presence of the main diffraction lines of the $\eta - Zn$ phase (JCPDS 01-2436) with the minor $ZnO$ (JCPDS 89-0511) impurities was detected in all tested samples. $PEG$ was present in the coated samples by two distinct peaks at 19.2° and 23.4°, while the low content of the Zn13Fe (JCPDS 01-0724) intermetallic phase was observed only in the spectrum of the uncoated $Zn-Fe$ samples.

Further confirmation of the presence of the polymer layer on the surface of the metal samples was provided by $EDX$ and Raman analysis. Only $Zn$ and $O$ were detected on the surface of the uncoated $Zn$ sample by $EDX$ analysis (**Figure 6a**). In addition, Fe was found on the surface of uncoated $Zn-Fe$ samples (**Figure 6b,c**). The existence of a $PEG$ layer on the surface of the coated samples was documented by the presence of carbon in the $EDX$ spectra of the coated samples (**Figure 6d-f**). $Zn$ and $Fe$ were not detected by $EDX$ at all due to the covering of the metal substrate with the layer of polymer coating.

The Raman spectra of all samples (uncoated and coated) together with the Raman spectrum for $PEG$ are shown in **Figure 6g**. Only the peak around 580 $cm^{-1}$ is present in the spectrum of all the uncoated samples ($Zn, Zn-1Fe$, and $Zn-2Fe$). This peak could be ascribed to the $A_1$ longitudinal optical ($LO$) photon and the $E_1$ ($LO$) vibration modes of $ZnO$ and indicates the intrinsic lattice defects.[37-39] The detection of the $PEG$ was demonstrated through the observation of multiple peaks in the spectrum of the $PEG$. Several very strong peaks appear in the Raman spectrum of pure $PEG$. A very strong specific doublet situated in the 830-880 $cm^{-1}$ region, assigned to $C-O-C$ stretching vibrations[40-42]; a high intense band at about 1280 $cm^{-1}$, which corresponds to $CH_2$ twisting[40,41,43]; a strong peak at about 1150 $cm^{-1}$ corresponding to $C-O$ stretching and $CH_2$ rocking vibra-tions[44,45]; and the medium Raman bands at about 1130 and 1500 $cm^{-1}$ due to the coupled vibration of $C-C$ and $C-O$ stretching[44,45] and the symmetric bending mode of the $CH_2$-$CH_2$ group,[43,45] respectively. The Raman spectra of all coated samples ($Zn + PEG, Zn-1Fe + PEG$ and $Zn-2Fe + PEG$) exhibit, in addition to the $ZnO$ peak, the characteristic bands assigned to $PEG$. The Raman bands at about 535, 1060, 1230 and 1460 $cm^{-1}$ are due to the $C-C-O$ bending vibration,[44] the $C-O$ stretching and $CH_2$ rocking vibrations,[44,45] the $CH_2$ twisting vibrations[44,45] and the $CH_2$-$CH_2$ anti-symmetric bending vibration,[44,45] respectively.

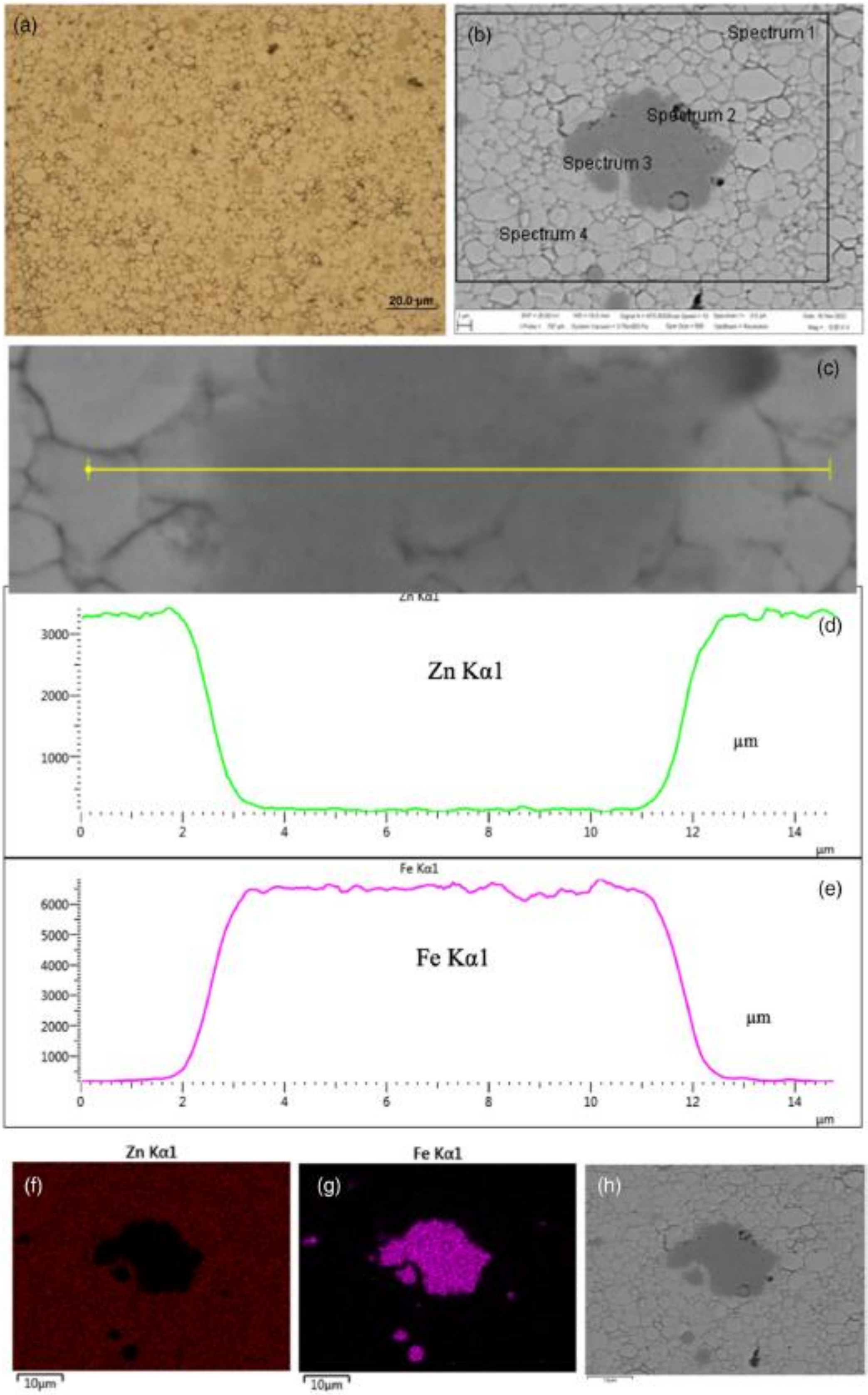

**FIGURE 4** Legend on next page.

***FIGURE 4*** *Micrographs and* $EDX$ *microanalysis of polished and etched sections through the interior of a sintered* $Zn-2Fe$ *sample; (a) light microscopy; (b)* $SEM$ *with the area and points of* $EDX$ *elemental analysis; (c)* $SEM$ *with the detail of the microstructure and the line of* $EDX$ *elemental microanalysis; (d) the distribution of* $Zn$ *from line* $EDX$ *analysis; (e) the distribution of Fe from line* $EDX$ *analysis; (f) the distribution of Zn from area* $EDX$ *analysis; (g) the distribution of* $Fe$ *from area* $EDX$ *analysis; (h)* $SEM$ *with the detail of the microstructure and the area of* $EDX$ *elemental microanalysis. [Color figure can be viewed at* ***wileyonlinelibrary.com****]*

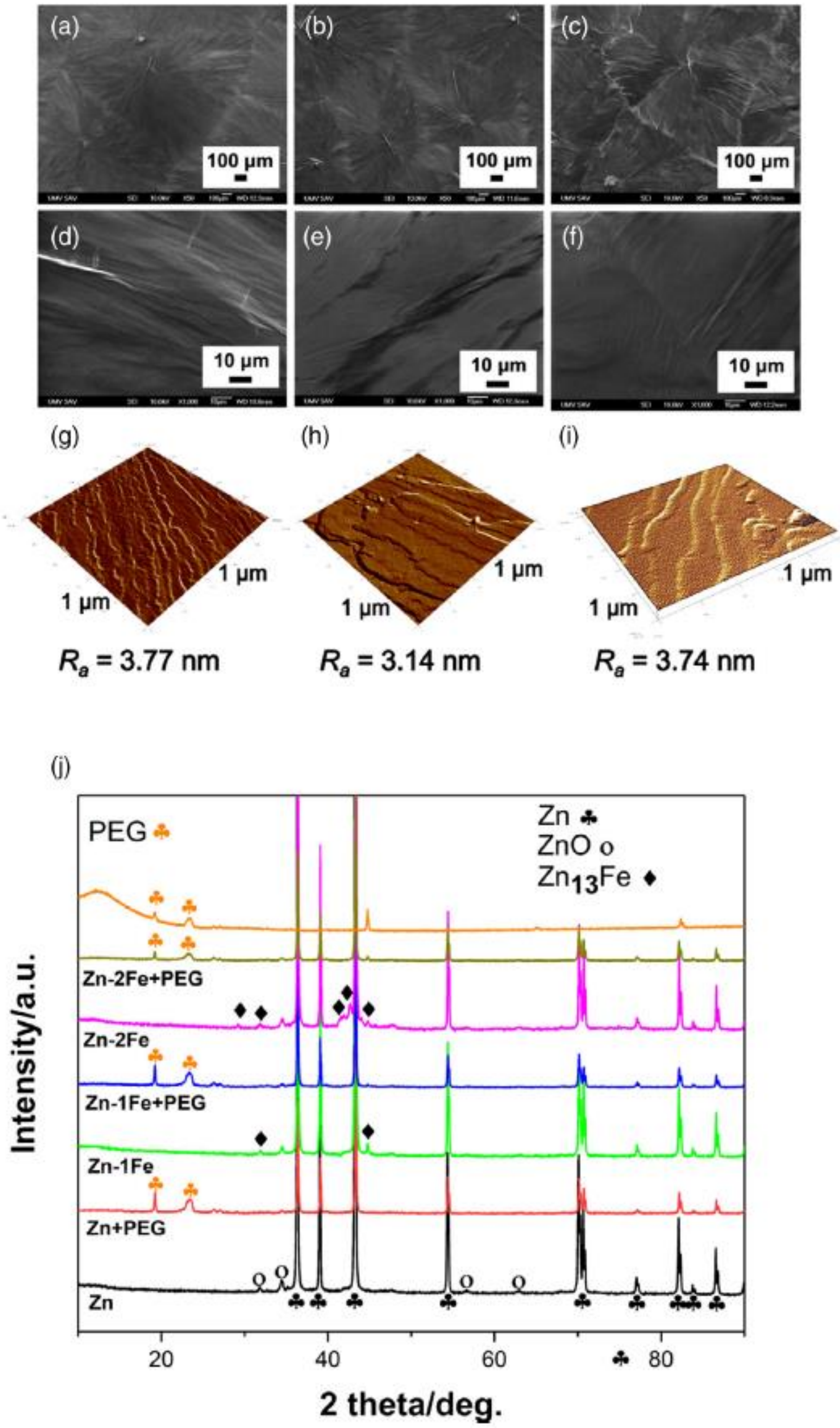
(a)
100 µm
(b)
100 µm
(c)
100 µm
(d)
10 µm
(e)
10 µm
(f)
10 µm
(g)
1 µm
1 µm
Ra = 3.77 nm
(h)
1 µm
1 µm
Ra = 3.14 nm
(i)
1 µm
1 µm
Ra = 3.74 nm
(j)
PEG ♣
Zn ♣
ZnO o
Zn13Fe ◆
Zn-2Fe+PEG
Zn-2Fe
Zn-1Fe+PEG
Zn-1Fe
Zn+PEG
Zn
Intensity/a.u.
20
40
60
80
2 theta/deg.

**FIGURE 5** $SEM$ images of the surface of $Zn\ +\ PEG$ (a, d), $Zn-1Fe+PEG$ (b, e) and $Zn-2Fe\ +\ PEG$ (c, f) samples; $AFM$ images and average surface roughness ($R_a$) values for $Zn\ +\ PEG$ (g), $Zn-1Fe+PEG$ (h) and $Zn-2Fe\ +\ PEG$ (i); $XRD$ spectrum of uncoated samples, $PEG$-coated samples and crystalline pure $PEG$ (j). [Color figure can be viewed at **wileyonlinelibrary.com**]

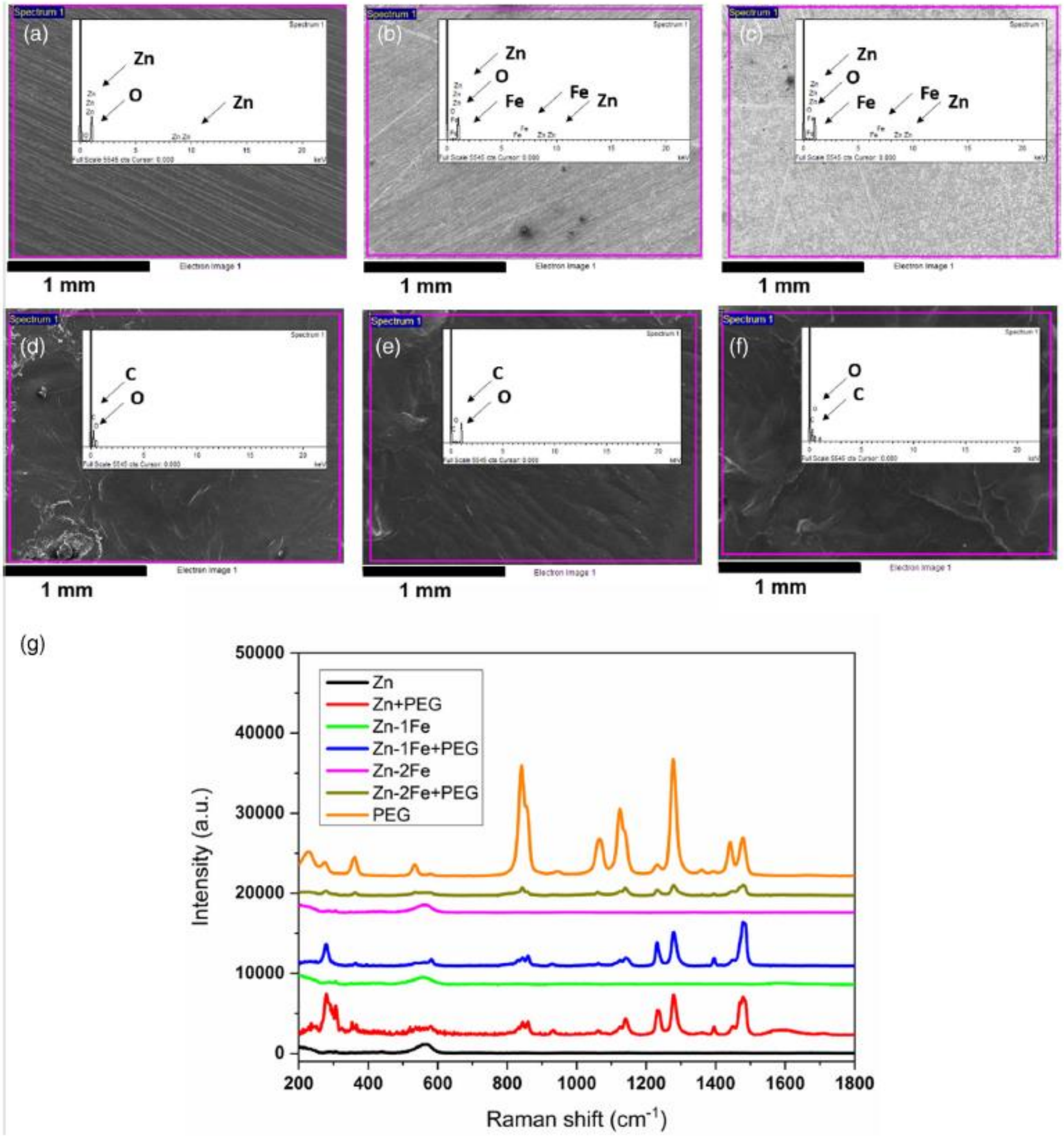

**FIGURE 6** $EDX$ analysis of the sample surface: $Zn$ (a), $Zn-1Fe$ (b), $Zn-2Fe$ (c), $Zn+PEG$ (d), $Zn-1Fe+PEG$ (e) and $Zn-2Fe+PEG$ (f). Raman spectrum of uncoated and $PEG$-coated zinc-based samples and pure $PEG$ (g). [Color figure can be viewed at **wileyonlinelibrary.com**]

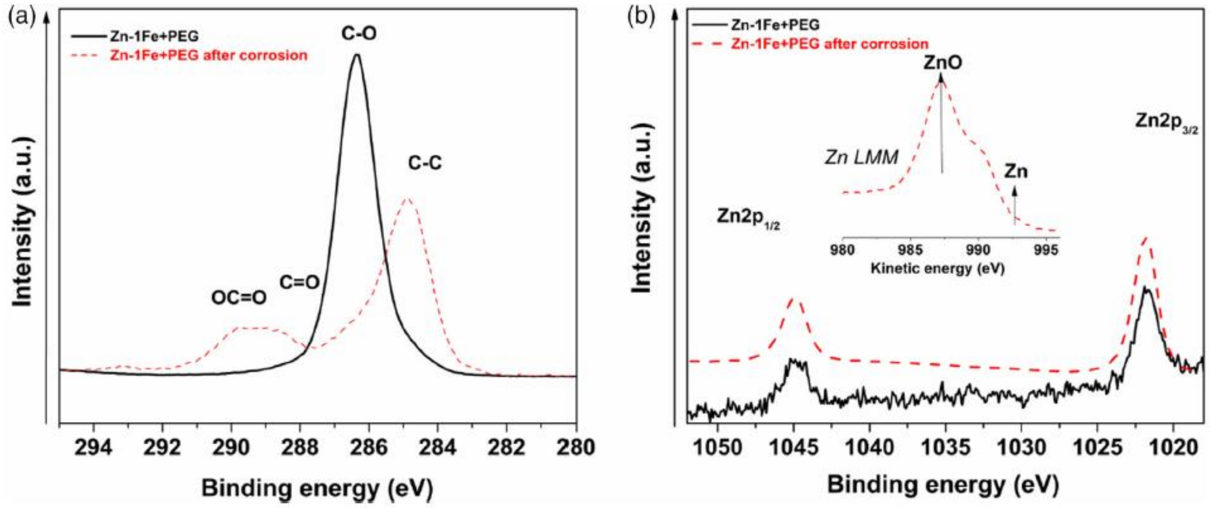

**FIGURE 7** $XPS$ spectra of the $Zn-1Fe\ +\ PEG$ sample of (a) C1s region and (b) $Zn2p$ region (inset is the $Zn\ LMM$ region of $Zn-1Fe\ +\ PEG$ after a 4-week immersion test in Hanks' solution). The black line corresponds to the as-prepared sample, and the red line corresponds to the sample after a 4-week immersion test in Hanks' solution. [Color figure can be viewed at **wileyonlinelibrary.com**]

The polymer layer was also confirmed using the $XPS$ technique by the presence of a C1s signal at ca. 286.3 eV corresponding to the $C-O$ bond in $PEG$ (**Figure 7a**, **Table 1**). Moreover, the formation of $ZnO$ was detected by $XPS$ analysis (**Figure 7**) in both pure $Zn$ and $Zn-Fe$ samples. In **Figure 7b**, the $Zn2p$ signal at 1021.8 eV corresponds to the $ZnO$ peak.[46] This is confirmed by the Zn LMM auger peak shown in the inset of Figure 7b, where the peak at 987.3 eV can be clearly assigned to the $ZnO$ compound, while there is no signal at 992 eV corresponding to $Zn$ metal. $Fe$ was visible only in the case of the $Zn-2Fe\ +\ PEG$ sample after corrosion, because the amount of iron was on the limit of the $XPS$ (0.1 at. %).

In theory, $XPS$ typically analyses a depth of 10 nm, providing information about the surface chemistry and electronic structure, while $XRD$ can penetrate the bulk of the material, within about 10 $\mu$m of the surface, providing information about the crystal structure of the entire sample.[47] Considering these limitations, the above results indicate that only $ZnO$ was present on the surface of the uncoated samples, while PEG was detected on the surface of the coated samples.

**TABLE 1** Apparent surface chemical composition as determined by $XPS$.

| | Surface chemical composition (at. %) | | | | |
|---|---|---|---|---|---|
| **Sample** | **C1s (C-O)** | **O1s** | **Zn2p3** | **Fe2p** | **Ca2p/P2s/Na1s/N1s/Mg1s/S2p** |
| Zn | 16.7 (1.5) | 54.5 | 15.2 | - | 2.6/9.1/0.5/–/1.4/– |
| Zn-1Fe | 20.1 (5.4) | 50.7 | 11.1 | - | 3.9/10.6/2.5/–/1.1/– |
| Zn-2Fe | 30.0 (7.2) | 47.6 | 15.1 | - | 0.8/4.8/0.2/0.9/0.6/– |
| Zn + PEG | 53.4 (31.5) | 36.4 | 8.9 | - | –/–/–/0.8/–/0.5 |
| Zn + PEG[a] | 28.4 (9.8) | 44.2 | 12.9 | - | 4.1/5.4/3.2/–/0.9/0.9 |
| Zn-1Fe + PEG | 67.4 (49.2) | 32.4 | 0.2 | - | –/–/–/–/–/– |
| Zn-1Fe + PEG[a] | 27.5 (2.9) | 46.9 | 13.9 | - | 2.6/5.1/2.0/1.1/0.9/– |
| Zn-2Fe + PEG | 67.9 (48.2) | 31.7 | 0.3 | - | –/–/0.1/–/–/– |
| Zn-2Fe + PEG[a] | 24.7 (1.5) | 48.7 | 20.9 | 0.1 | 1.4/–/3.5/–/0.7/– |

[a] *After a 4-week immersion test in Hanks' solution.*

The bulk material (subsurface layers) of prepared $Zn$ and $Zn-Fe$ sintered samples is mainly composed of $\eta-Zn$ phase with minor $ZnO$ impurities at the boundaries of the zinc particles. In addition, the low content of the $Zn_{13}Fe$ intermetallic phase was detected in the $Zn-Fe$ samples. This secondary phase is probably localized at the boundaries of the iron particles. This assumption is supported by the results of the line $EDX$ analysis shown in **Figures 3d,e** and **4d,e**, according to which the simultaneous occurrence of $Fe$ and $Zn$ is observed at particle boundaries. This is favorable from the point of view of using prepared materials for biodegradable implants because the $Zn_{13}Fe$ alloy worsens the mechanical properties and degradability of $Zn-Fe$ biomaterials.[48]

### *3.2 Corrosion behavior*

Although $Zn$ biomaterials exhibit higher corrosion rates than iron ones, their degradation is still slow for many biomedical applications.[3] Acceleration of corrosion of $Fe$ biomaterials due to a $PEG$ coating was explained in our previous papers.[29-32] Therefore, the possibility of increasing the corrosion rate of $Zn$ and $Zn-Fe$ materials using a $PEG$ coating layer was studied in this work.

A comparison of the apparent surface chemical composition determined by $XPS$ before and after corrosion shows that the $PEG$ coating layer was decomposed after a 4-week immersion in Hanks' solution. The $PEG$ layer was clearly visible before corrosion, but after corrosion, the C1s signal of $C-O$, representing $PEG$, readily decreased (**Figure 7a**, **Table 1**). Moreover, the $Zn2p$ signal corresponding to the $ZnO$ peak increased after corrosion, indicating the diminishing of the $PEG$ polymer layer.

The surface morphologies, together with the composition of the surface of corroded samples after a 4-week immersion in Hanks' solution, are shown in **Figure 8**. Optical images (inserts in **Figure 8a-f**) indicate a relatively uniform corrosion mechanism macroscopically. SEM micrographs indicate a higher extent of corrosion for the polymer-coated samples, with a cracked layer of corrosion products. While uniform corrosion was observed for the uncoated samples, a few aggregates of corrosion products can be seen on the surface of the polymer-coated samples. The uniform corrosion attack at the external surface of the $Zn-Fe$ alloy was also revealed by Kafri et al.[16] A uniform corrosion mechanism is one of the important properties required from implantable degradable biomaterials.

Based on $EDX$ analysis, precipitation of the corrosion products formed predominantly by $Zn$, $Fe$, $O$, $P$ and $Ca$ elements could be observed on sample surfaces, indicating that the degradation products are mainly composed of zinc and iron hydroxides, phosphates, and calcium phosphates. This is in accordance with results reported in the current literature.[11,24,29,49-53] However, from the very low iron content in $EDX$ spectra as well as from the results of $XPS$ and $XRD$ (see below) analyses, it follows that insoluble $Zn$ compounds dominate in the corrosion products.

The average values of the density of the samples, which were determined from the measured dimensions and weight of the samples, are shown in **Table 2**. The density increased with increasing $Fe$ content. The $PEG$-coated samples showed a higher density than the uncoated samples. Values of the corrosion rates determined from mass loss after a 4-week immersion in Hanks' solution are summarized in **Table 2**. An increase in the degradation rate with an increase in iron content was observed. Furthermore, the $PEG$-coated samples exhibited slightly higher corrosion rates as compared to uncoated samples. The cracked layer of corrosion products due to the change in pH after the dissolution of the $PEG$ layer plays an important role in increasing the corrosion rate. A local decrease in the pH value near the surface of the samples with $PEG$ leads to the formation of a less dense, porous and cracked layer of degradation products, which allows corrosion to continue and does not act as passivating, as in the case of samples without $PEG$.[31,32]

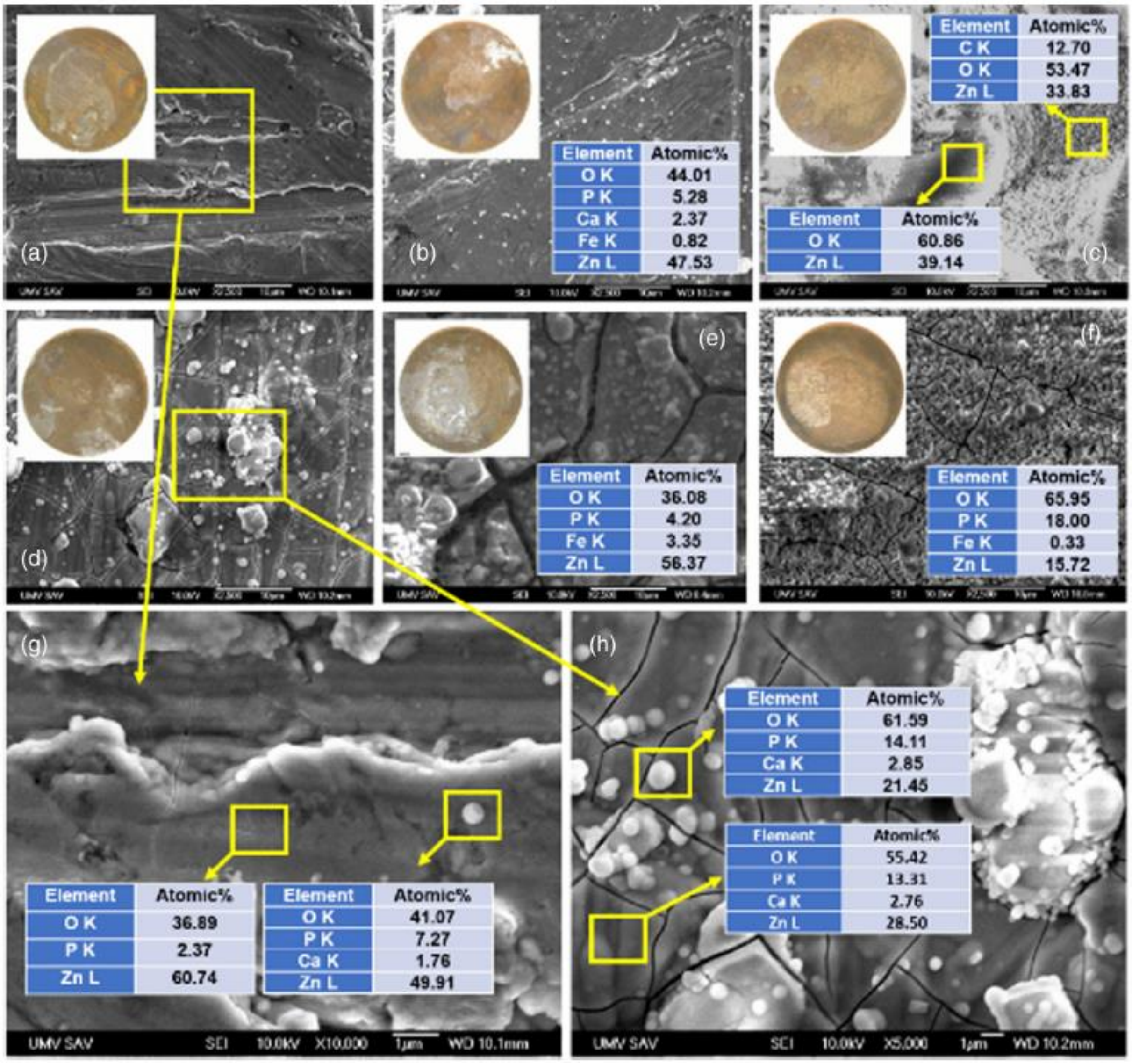

**FIGURE 8** $SEM$ analysis coupled with $EDX$ analysis of corrosion deposits created on $Zn$-based (uncoated and $PEG$-coated) samples after 4 weeks of degradation in Hanks' solution. $Zn$ (a), $Zn-1Fe$ (b), $Zn-2Fe$ (c), $Zn + PEG$ (d), $Zn-1Fe + PEG$ (e), $Zn-2Fe + PEG$ (f) and details from pure Zinc (g) and $PEG$-coated zinc (h). [Color figure can be viewed at **wileyonlinelibrary.com**]

**TABLE 2** Average values of density and corrosion rates determined from mass loss after a 4-week immersion in Hanks' solution.

| Sample | Density (g cm$^{-3}$) | Mass loss (mg) | *CR* (mm year$^{-1}$) |
|---|---|---|---|
| Zn | 6.342 | 0.556 | 0.00339 ± 0.0003 |
| Zn + PEG | 6.372 | 0.622 | 0.00380 ± 0.0005 |
| Zn-1Fe | 6.390 | 1.054 | 0.00630 ± 0.0004 |
| Zn-1Fe + PEG | 6.414 | 1.327 | 0.00793 ± 0.0009 |
| Zn-2Fe | 6.468 | 1.114 | 0.00683 ± 0.0006 |
| Zn-2Fe + PEG | 6.522 | 1.206 | 0.00723 ± 0.0009 |

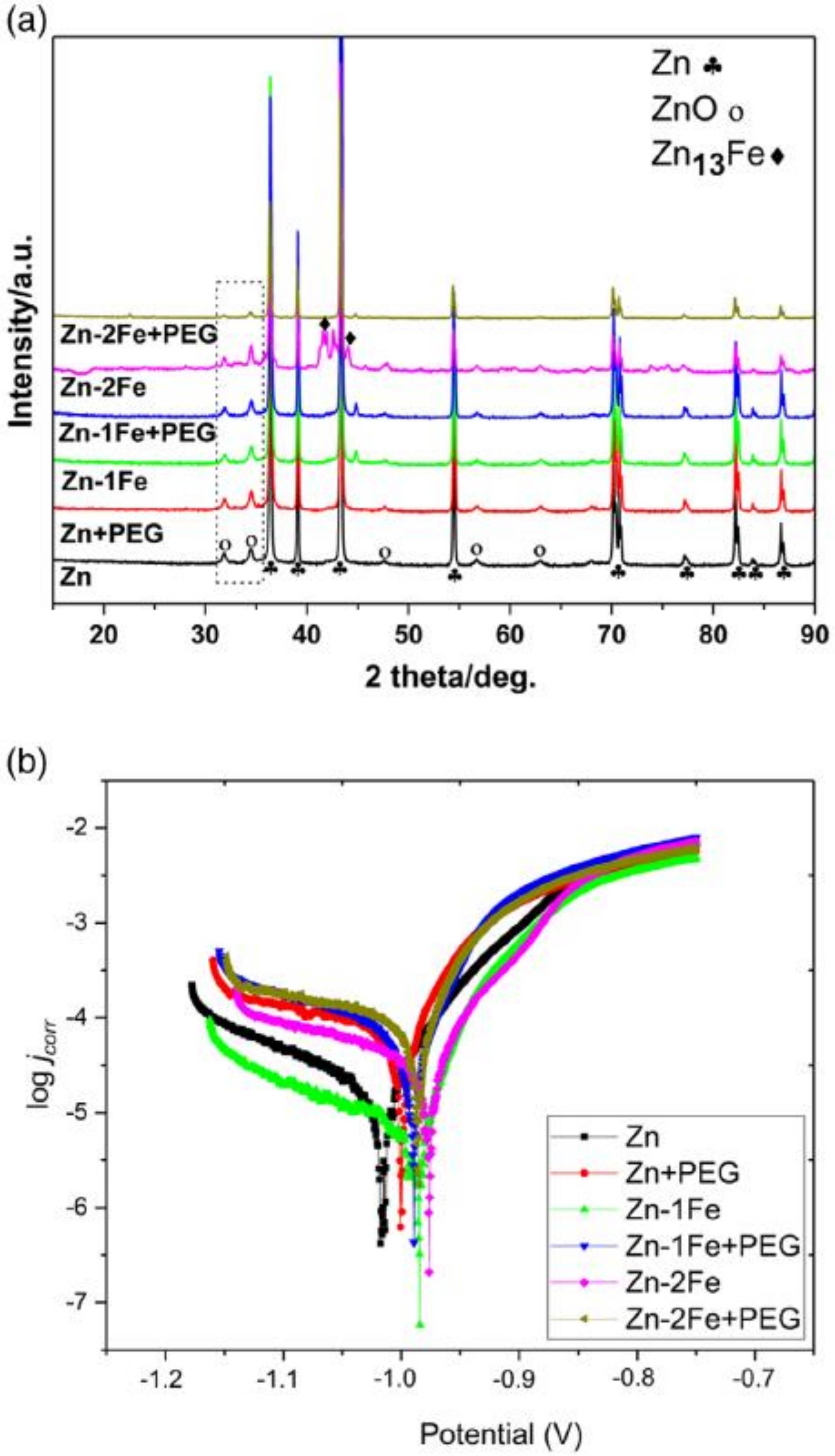

**FIGURE 9** Representative potentiodynamic polarization curves registered in Hanks' solution (a). $XRD$ analysis of $Zn$-based samples corroded for 4-weeks in the Hanks' solution (b). [Color figure can be viewed at **wileyonlinelibrary.com**]

In addition to elemental analysis, $XRD$ analysis was performed to confirm the presence and to analyze the composition of corrosion products formed on the surface of samples after a 4-week immersion in Hanks' solution. The $XRD$ patterns of the studied samples after immersion in Hanks' solution are shown in **Figure 9a**. The $PEG$ lines have completely vanished from the $XRD$ patterns. Moreover, an increase in the intensity of the ZnO phase was found in all spectra, and the lines for $Zn_{13}Fe$ were more pronounced in the $Zn-2Fe$ alloy in comparison with the patterns before corrosion. These results are in line with the results of the $XPS$ analysis of the corroded samples (**Figure 7**, **Table 1**).

An electrochemical study was further conducted to evaluate the corrosion properties of the prepared samples. Representative potentiodynamic polarization curves of the samples in Hanks' solution are presented in **Figure 9** and electrochemical parameters calculated using Tafel extrapolation are summarized in **Table 3**. The course of the polarization curves is similar for all the studied samples. The spontaneous passivation occurs on the anodic side, while the hydrogen evolution reaction is visible on the cathodic region. The determined values of average corrosion potential are very close. The corrosion potential shifted from -1.028 V for a bare Zn sample to -0.988 V for $Zn-2Fe+PEG$, indicating an increase in the thermodynamic stability of the samples with a minor addition of iron and a polymer coating. Also, the polymer coating led to a shift of the corrosion potential to less negative values compared to the samples without the $PEG$ layer.

The calculated corrosion rates show acceleration of degradation with increasing $Fe$ content for both uncoated and coated samples. The reduced corrosion rate of bare Zn biomaterials as compared to $Zn-Fe$ materials was reported earlier in vitro[16,17,33] and in vivo.[54] As reported previously, the corrosion rates of $Zn$-based materials are higher when compared to bare $Zn$ due to the micro galvanic corrosion behavior between the $Zn$ (anode) and its secondary phase (cathode).**17,53,55-57** In general, the $PEG$-coated samples exhibited higher corrosion rates than uncoated samples. This trend was also observed for immersion corrosion, but for the electrochemical test, the rate increase was much more pronounced. While a slight increase in the degradation rate was observed for the $Zn$ sample (~1.2 times), a more significant increase in the corrosion rate was detected for the $Zn-Fe$ samples (more than 2 times) after polymercoating deposition, revealing a synergic effect of $Fe$ and $PEG$ on the degradation rate. The $Zn-2Fe+PEG$ sample exhibited the highest corrosion rate among all the tested samples. A similar effect of $PEG$ coating on the corrosion rate of $Fe$-based materials was previously reported,[29,30,32] and acceleration of degradation of iron biomaterials by a polylactide ($PLA$) and poly(lactic-co-glycolic acid) ($PLGA$) coating was observed by Qi[58] and Yusop,[59] respectively.

**TABLE 3** Electrochemical corrosion parameters measured in Hanks' solution at 37° C with a 0.1 mV s 1 scan rate.

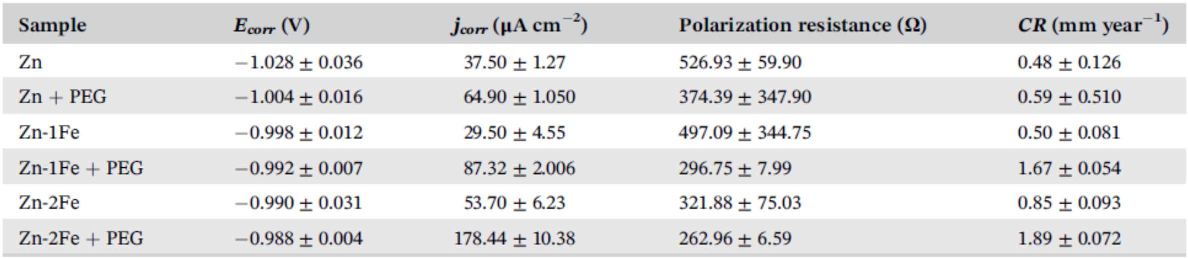

| Sample | $E_{corr}$ (V) | $j_{corr}$ (µA cm$^{-2}$) | Polarization resistance (Ω) | $CR$ (mm year$^{-1}$) |
|---|---|---|---|---|
| Zn | −1.028 ± 0.036 | 37.50 ± 1.27 | 526.93 ± 59.90 | 0.48 ± 0.126 |
| Zn + PEG | −1.004 ± 0.016 | 64.90 ± 1.050 | 374.39 ± 347.90 | 0.59 ± 0.510 |
| Zn-1Fe | −0.998 ± 0.012 | 29.50 ± 4.55 | 497.09 ± 344.75 | 0.50 ± 0.081 |
| Zn-1Fe + PEG | −0.992 ± 0.007 | 87.32 ± 2.006 | 296.75 ± 7.99 | 1.67 ± 0.054 |
| Zn-2Fe | −0.990 ± 0.031 | 53.70 ± 6.23 | 321.88 ± 75.03 | 0.85 ± 0.093 |
| Zn-2Fe + PEG | −0.988 ± 0.004 | 178.44 ± 10.38 | 262.96 ± 6.59 | 1.89 ± 0.072 |

While the susceptibility of material to corrosion is given by thermodynamic stability, the rate of corrosion depends on kinetic parameters.[51] Lower polarization resistance corresponds to faster degradation.[60] At the beginning of the corrosion test, the intact compact $PEG$ layer acted as a barrier against corrosion, which was reflected in higher thermodynamic stability (less negative corrosion potential). As a result of the degradation of the $PEG$ layer, there was a decrease in the pH around the samples, which caused the formation of a cracked and porous layer of corrosion products. Through these pores and cracks, the contact of the corrosive medium with the surface of the biomaterial was enabled and electrochemical reactions took place in the interface between the metal and the electrolyte, which led to an acceleration of corrosion of $PEG$ coated samples as compared to uncoated samples.[29,30,32] Moreover, the formation of local galvanic micro-cells between the $Zn$ (anode) and its secondary phase (cathode) leads to an acceleration of the corrosion of $Zn - Fe$ samples compared to $Zn$ samples. , , The metal is oxidized at the anodes, whereas the corrosion process is maintained by the reduction of oxygen from the electrolyte at the cathodes.[61] The combination of both effects resulted in an increase in the degradation rate of $Zn$-based biomaterials.

In general, the electrochemical corrosion of zinc and iron in a neutral physiological environment proceeds via cathodic and anodic reactions[7,13,16,18,29,33,51,53,59,62] and subsequent products formation:

$$\text{Anodic reactions}: Zn \rightarrow Zn^{2+} + 2e^{-} \tag{3}$$

$$Fe \rightarrow Fe^{2+} + 2e^{-} \tag{4}$$

$$\text{Cathodic reaction}: O_2 + 2H_2O + 4e^{-} \rightarrow 4OH^{-} \tag{5}$$

$$\text{Subsequent reactions}: Zn^{2+} + 2OH^{-} \rightarrow Zn(OH)_2 \tag{6}$$

$$Zn(OH)_2 \rightarrow ZnO + H_2O \tag{7}$$

$$Fe^{2+} + 2OH^{-} \rightarrow Fe(OH)_2 \tag{8}$$

$$Fe^{2+} \rightarrow Fe^{3+} + e^{-} \tag{9}$$

$$Fe^{3+} + 3OH^{-} \rightarrow Fe(OH)_3 \tag{10}$$

The passive layer of corrosion products is formed primarily by the products of reactions (**6**) to (**10**),[7] but as was supported by the presented results, the passive layer in this study is formed mainly by the products of reactions (**6**) and (**7**). It is likely that iron compounds were also formed, but their amounts were below the detection limit.

Hydrolysis of $Fe(OH)_3$ can take place in solutions containing oxygen and chloride anions to form goethite ($FeO(OH)$), which partially reacts with $Fe(OH)_2$[29,62]:

$$2\,FeO(OH) + Fe(OH)_2 \rightarrow Fe_3O_4 + H_2O \qquad (11)$$

In Hanks' solution, which contains a large amount of chloride anions, the following reactions can also take place[7,13,18,33,51]

$$Zn^{2+} + 2\,Cl^- + 6\,Zn(OH)_2 \rightarrow 6\,Zn(OH)_2.ZnCl_2 \qquad (12)$$

$$Zn^{2+} + 2\,Cl^- + 4\,ZnO + 4\,H_2O \rightarrow 4\,Zn(OH)_2.ZnCl_2 \qquad (13)$$

$$Fe(OH)_2 + Cl^- \rightarrow FeClOH + OH^- \qquad (14)$$

$$FeClOH + H^+ \rightarrow Fe^{2+} + Cl^- + H_2O \qquad (15)$$

$$Fe(OH)_3 + 2\,Cl^- \rightarrow FeCl_2OH + 2\,OH^- \qquad (16)$$

$$FeCl_2OH + H^+ \rightarrow Fe^{3+} + 2\,Cl^- + H_2O \qquad (17)$$

In addition, phosphates and carbonates are formed in Hanks' solution[7,13,33,53]:

$$3\,Zn^{2+} + 2\,HPO_4^{2-} + 2\,OH^- + 2\,H_2O \rightarrow Zn_3(PO_4)_2(H_2O)_4 \qquad (18)$$

$$5\,Zn^{2+} + 2\,HCO_3^- + 8\,OH^- \rightarrow Zn_5(CO_3)_2(OH)_6 + 2\,H_2O \qquad (19)$$

$$2\,PO_4^{3-} + 3\,Ca^{2+} \rightarrow Ca_3(PO_4)_2\downarrow \qquad (20)$$

$$6\,PO_4^{3-} + 10\,Ca^{2+} + 2\,OH^- \rightarrow Ca_{10}(PO_4)_6(OH)_2\downarrow \qquad (21)$$

$$2\,PO_4^{3-} + 3\,Fe^{2+} + 8\,H_2O \rightarrow Fe_3(PO_4)_2.8\,H_2O \qquad (22)$$

$$PO_4^{3-} + Fe^{3+} \rightarrow FePO_4 \downarrow \tag{23}$$

The corrosion of coated samples is affected by the dissolution of polymer in Hanks' solution and the presence of $PEG$ oligomers and their subsequent degradation by the oxidative mechanism. The cracks and defects in the dissolving coating layer allow the interaction of the corrosion medium with the surface of the material and thus its corrosion. $PEG$ degradation starts with oxidation of the terminal $OH$ group and hydrogen atom splitting, causing a decrease in the pH of the solution.[29,63,64] Interaction between the polymer and water also caused a change in pH[29,65,66]:

$$HO(CH_2CH_2O)_nH + H_2O \rightleftharpoons H_30^+ + HO(CH_2CH_2O)_n^- \tag{24}$$

A local decrease in the pH value near the surface of the $PEG$-coated samples leads to increased solubility of the corrosion products and the formation of a less compact and dense passive layer, thus accelerating their degradation.

Moreover, the complexing of iron ($Fe^{3+}$) by $PEG$ was reported[63,64]:

$$mHO(CH_2CH_2O)_nH + Fe^{3+} \rightleftharpoons mH^+ + \left(\left[HO(CH_2CH_2O)_n\right]_m Fe\right)^{3-m+} \tag{25}$$

After formation, $Fe^{3+}/PEG$ complexes diffuse in solution. In addition to the low $Fe$ content, this could be another reason for the low Fe content in the corrosion product layer on the surface of the samples. According to H. Boudellioua,[67] reaction (**25**) hinders the formation of corrosion products.

### *3.3 In vitro cytocompatibility*

The relative viability of $HDFa$ cells after culturing in the extracts of the studied samples for 4 and 24 h at different concentrations (100%, 50%, and 10%) are shown in **Figure 10** and listed in **Table 4**. Generally, after 4 h of incubation, the cell viability was above 84% compared to the blank control group for all the samples and concentrations of the extracts, thus revealing good biocompatibility. Moreover, a slight positive effect of the polymer coating on the cell viability was observed. Among the studied samples, the bare $Zn$ samples showed the highest increase in cell viability after $PEG$ coating. The undiluted extracts exhibited relative viability in the range from 84.79% to 91.90%. When the concentration of the extracts was diluted to 10%, the relative viability was approximately 3%-6% higher (ranging from 88.48% to 93.87%). The $HDFa$ cells cultured in the extracts of $Zn + PEG$ sample showed the highest viability among all the studied samples, which was above 90% even in an undiluted extract medium.

After 24 h of incubation, only the extracts of the $Zn$ sample showed a relative viability of $HDFa$ cells above 80%. This is probably the result of faster corrosion of the samples with iron content and with a polymer coating and the related change in pH and the accumulation of degradation products. However, cell viability does not fall below 60% in any extract.

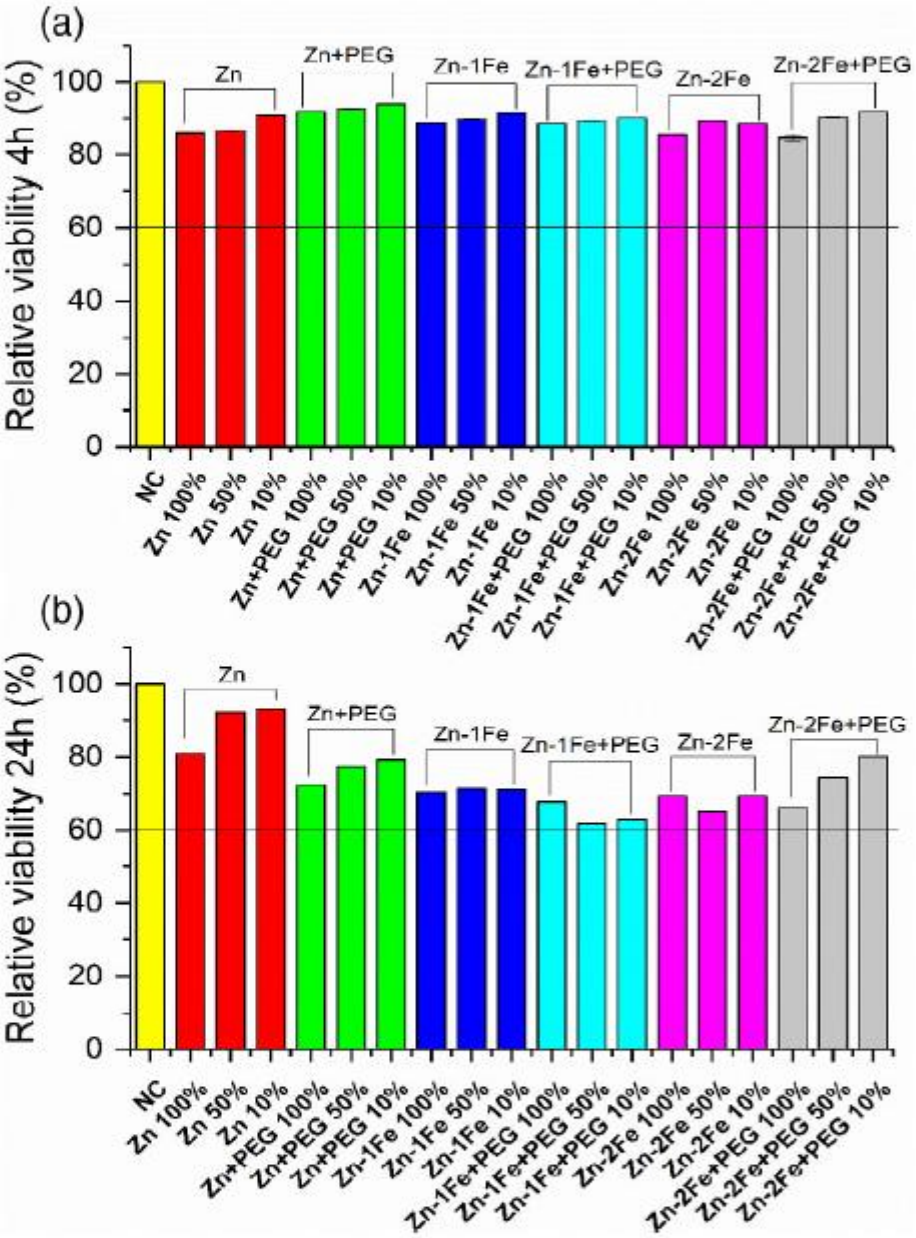

**FIGURE 10** Relative viability of $HDFa$ cells obtained from the $MTS$ assay. [Color figure can be viewed at **wileyonlinelibrary.com**]

**TABLE 4** Relative viabilities of $HDFa$ cells tested with 100%, 50% and 10% concentration of sample extracts.

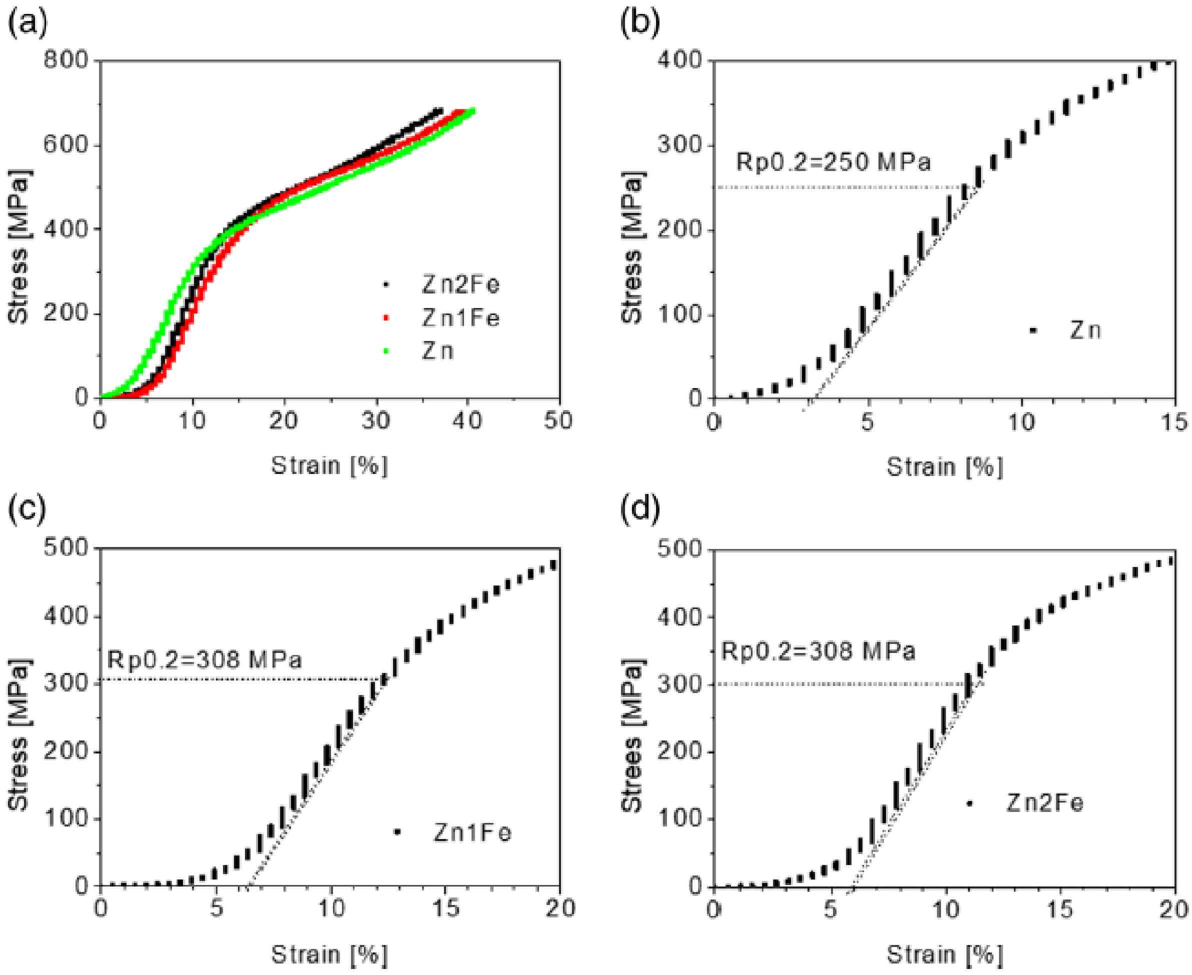

**FIGURE 11** (a) A plot of stress versus strain during the compression test; determination of the compressive 0.2% proof stress of the (b) $Zn$ sample, (c) $Zn-1Fe$ sample and (d) $Zn-2Fe$ sample. [Color figure can be viewed at **wileyonlinelibrary.com**]

Following ISO 10993-5 (2009), a reduction of cell viability by more than 30% is considered a cytotoxic effect.[36] In this work, the largest drop in viability after 4 h, ~15%, was observed for the cell cultures exposed to the undiluted extract of the $Zn-2Fe$ sample, and therefore the prepared materials can be considered cytocompatible. After 24 h of incubation, a decrease in relative cell viability below 70% was recorded for the extracts of the $Zn-2Fe$ and $Zn-1Fe+PEG$ samples for all concentrations of the extracts and for the undiluted extract of the $Zn-2Fe+PEG$ sample. These samples therefore do have a cytotoxic effect on $HDFa$ cells.

### *3.4 Mechanical properties*

In our previous works, an improvement in the mechanical properties of $Fe$-based biomaterials was observed after the deposition of a polymeric $PEG$ layer.[29-32] However, the influence of the polymer coating on the mechanical behavior of $Zn$-based biomaterials has not been studied yet. Therefore, a preliminary study of the mechanical properties of these materials was performed in this work.

A uniaxial compression test was first performed on all three groups of uncoated material ($Zn$, $Zn-1Fe$ and $Zn-2Fe$) to determine their conventional stress-strain behavior and compressive 0.2% proof stress (**Figure 11**).

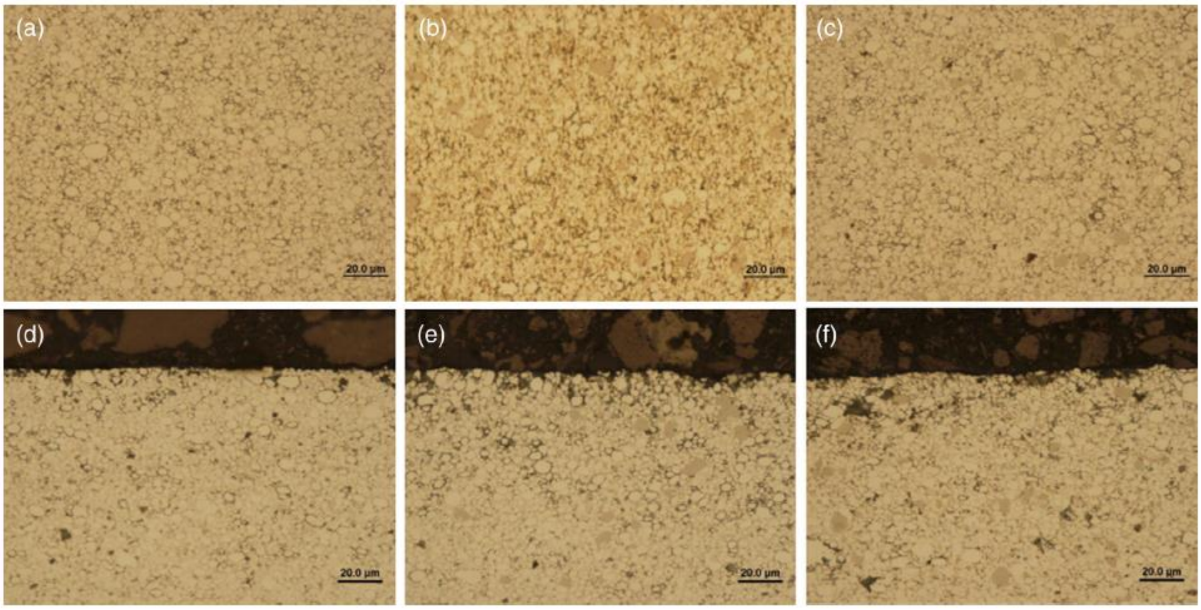

**FIGURE 12** The microstructure of uncoated samples before compression testing: (a) $Zn$ sample, (b) Zn-1Fe sample, (c) $Zn-2Fe$ sample and after compression testing, (d) $Zn$ sample, (e) $Zn-1Fe$ sample and (f) $Zn-2Fe$ sample. [Color figure can be viewed at **wileyonlinelibrary.com**]

The $Zn$ samples had an average value of 0.2% proof stress of about 250 MPa, while both $Zn-1Fe$ and $Zn-2Fe$ samples had a 0.2% proof stress value of 308 MPa (**Figure 11b-d**).

Plastic deformation caused the microstructure of the samples to change from that consisting of mostly globular $Zn$ grains to that containing ellipsoidal grains (**Figure 12**). No plastic deformation was observed in the subsurface area in the $Zn$ samples, and local de-cohesion of the $Zn$ grains was noted up to a depth of 10 $\mu$m (**Figure 12d**). In the $Zn-1Fe$ samples, matrix integrity was compromised to a depth of 20 $\mu$m under the surface after the compression test (**Figure 12e**). No plastic deformation of the $Fe$-based grains was observed (**Figure 12e**). In the $Zn-2Fe$ samples, de-cohesion of the $Fe$-based particles from the $Zn$ matrix was observed up to a depth of 20 $\mu$m (**Figure 12f**). The stress-strain diagrams indicated that all three sample groups exhibited linear work hardening throughout the plastic deformation (**Figure 11a**).

The $Zn-Fe$ materials exhibit a slightly higher 0.2% proof stress compared to pure zinc. Enhancement of the mechanical properties of $Zn-Fe$ materials is believed to be the result of the presence of iron particles within the material, which are not present in pure zinc. The iron particles can make a material stronger due to their higher hardness and stiffness, which leads to increased resistance to plastic deformation. Furthermore, the iron particles serve as a reinforcement, physically restricting the movement of dislocations and thus further enhancing the material's ability to resist plastic deformation.

The $PEG$-coated $Zn$, $Zn-1Fe$ and $Zn-2Fe$ samples underwent a uniaxial compression test to determine their conventional stress-strain behavior and 0.2 proof stress (**Figure 13a**). The average value of the 0.2% proof stress was found to be 214 MPa for the $Zn + PEG$ system, 170 MPa for the $Zn-1Fe + PEG$ system and 168 MPa for the $Zn-2Fe + PEG$ system (**Figure 13b-d**). The plastic deformation caused the microstructure of the samples to change from that consisting of mostly globular $Zn$ grains to that also containing ellipsoidal grains (**Figure 14**). The $PEG$ layer, which was compact and intact before the test (**Figure 14a-c**), was not observed by light microscope after the compression test (**Figure 14d-f**). After the compression test, an intense plastic deformation was observed up to a depth of 10 $\mu$m for the $Zn - PEG$ samples. There was no cracking or breach in the integrity of the $Zn + PEG$ material throughout the entire volume of the sample (**Figure 14d**). After the compression test on the samples of the $Zn - 1Fe + PEG$ material, the cracking in the $Zn$ matrix was observed up to a depth of 5 $\mu$m (**Figure 14e**). No plastic deformation of the $Fe$-based grains was observed (**Figure 14e**). According to the plot of the stress versus strain, the $Zn - 1Fe + PEG$ type material is not significantly hardened for a plastic strain in the range from 0.2% up to 10% (**Figure 13a**). In the $Zn - 2Fe + PEG$ samples, de-cohesion of the $Fe$-based grains from the $Zn$ matrix was observed in the plastically deformed zone reaching up to a depth of 20 $\mu$m (**Figure 14f**). The stress-strain curve for the $Zn - 2Fe + PEG$ samples shows that this material is not significantly strengthened within the plastic strain range from 0.2% to 17% (**Figure 13a**).

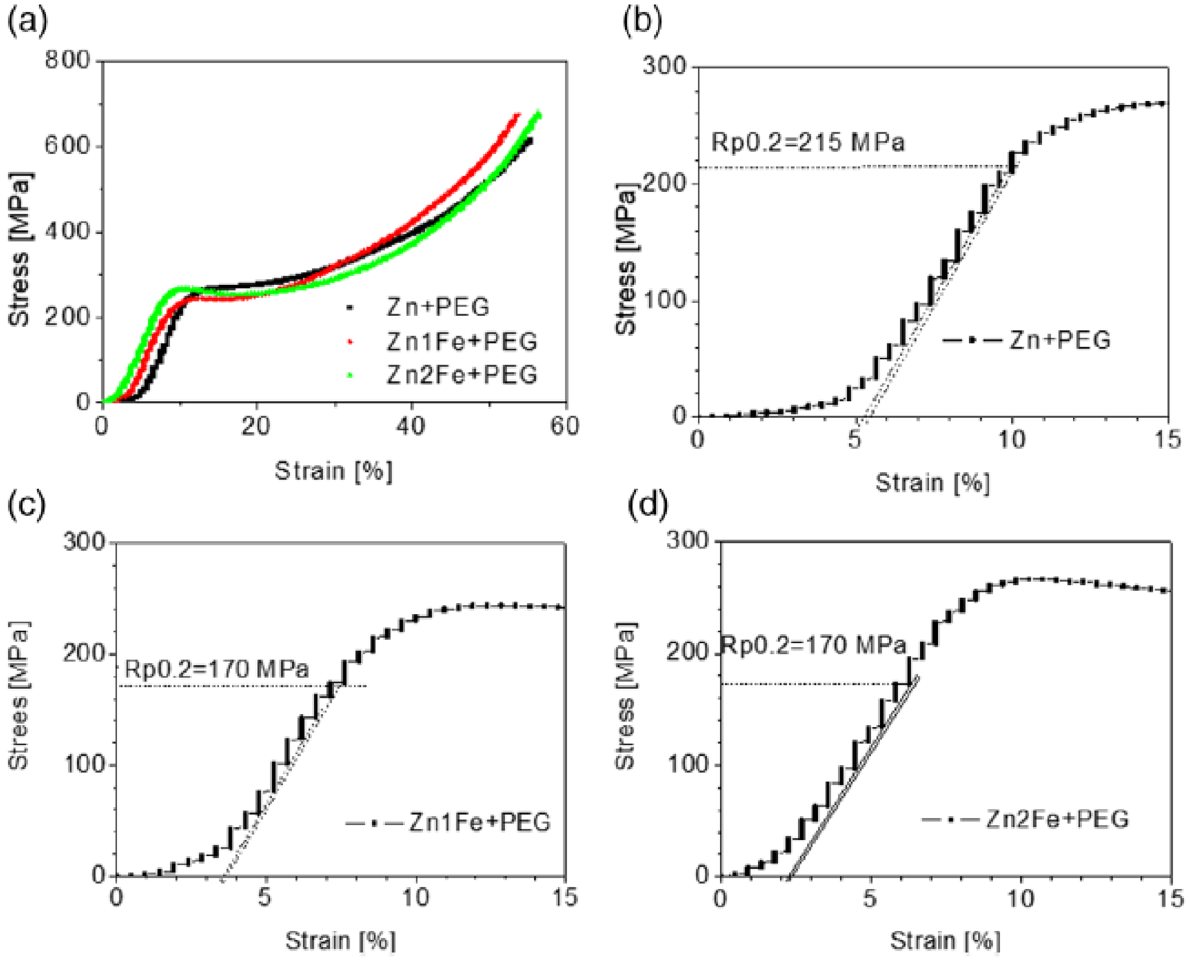

**FIGURE 13** (a) A plot of stress versus strain during the compression test; determination of the compressive 0.2% proof stress of the (b) $Zn + PEG$ system, (c) $Zn - 1Fe + PEG$ system and (d) $Zn - 2Fe + PEG$ system. [Color figure can be viewed at **wileyonlinelibrary.com**]

The stress-strain curves showed (**Figure 13**) that the $Zn + PEG$, $Zn - 1Fe + PEG$ and $Zn - 2Fe + PEG$ samples are not significantly strengthened for plastic strains of at least up to 10%. This means that these materials can undergo additional pressure-induced plastic deformation without significant strengthening. This property provides the possibility of further shaping of a potential implant, which is an important consideration in biomedical applications. However, for a deeper understanding of the mechanical behavior of polymer-coated $Zn$-based biomaterials, further studies are needed.

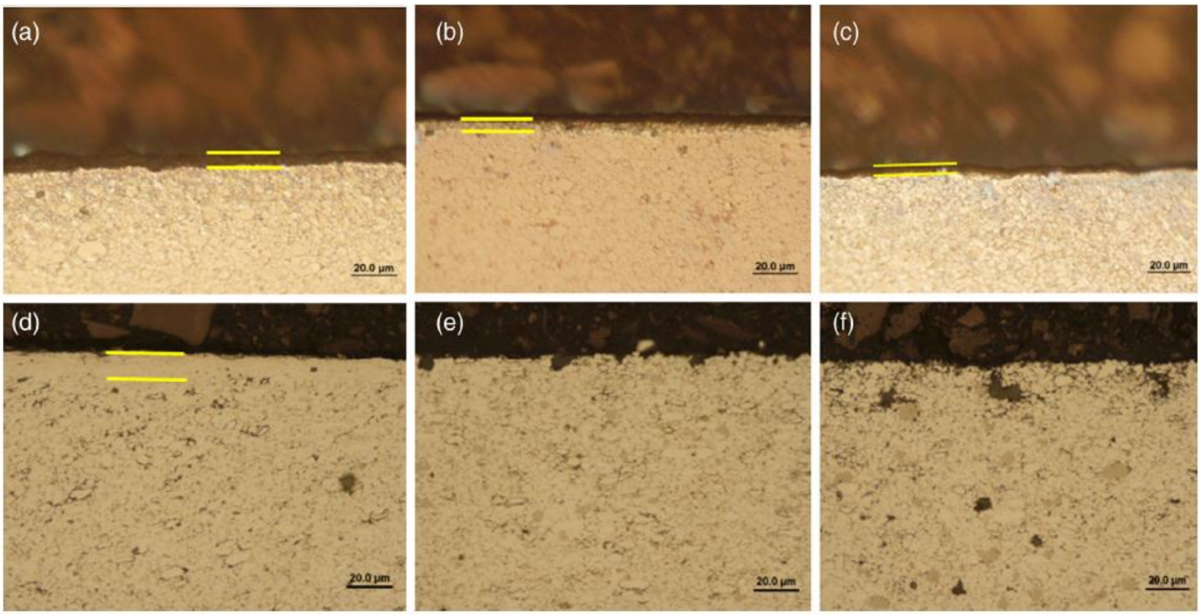

**FIGURE 14** The microstructure of the coated samples before compression testing of the (a) $Zn + PEG$ sample, (b) $Zn - 1Fe + PEG$ sample, (c) $Zn - 2Fe + PEG$ sample and after compression testing of the (d) $Zn + PEG$ sample, (e) $Zn - 1Fe + PEG$ sample and (f) $Zn - 2Fe + PEG$ sample. [Color figure can be viewed at **wileyonlinelibrary.com**]

## 4 CONCLUSIONS

In this study, biodegradable $Zn$-based materials were studied regarding their microstructure, corrosion behavior, mechanical properties and biocompatibility. The concurrent influence of minor Fe addition to $Zn$ and polyethylene glycol coating was evaluated.

The sintered samples were mainly composed of $\eta - Zn$ phase with a low content of $ZnO$ at the boundaries of zinc particles, and the intermetallic phase $Zn_{13}Fe$. Only the presence of $ZnO$ was observed on the outmost surface of all uncoated metallic samples, while the $PEG$ was present on the surface of the coated samples resulting in a decrease in surface roughness.

An increase in the degradation rate due to both iron addition and $PEG$ coating was observed. However, a decrease in cell viability was registered for Fe-containing samples as compared to pure $Zn$ samples. After 24 h of incubation, a decrease in viability below 70% was registered as the result of the combined effect of Fe and $PEG$. The $Zn + PEG$ sample showed the highest viability. An improvement in mechanical properties was observed for uncoated $Zn - Fe$ samples due to the presence of iron particles within the material. The $PEG$-coated $Zn - Fe$ samples were not significantly strengthened within the plastic strain range and can undergo additional plastic deformation induced by pressure without significant strengthening, which provides the possibility of further shaping of a potential implant.

The properties of the $Zn - Fe$ material can be tuned through the content of $Fe$ and the coating with a polymer coating. The produced $Zn$-based materials exhibit great potential for biomedical applications.

## REFERENCES

[1] S. Wei, J.-X. Ma, L. Xu, X.-S. Gu, X.-L. Ma, Mil. Med. Res. **2020**, 7, 54.

[2] P. Habibovic, Tissue Eng. Part A **2017**, 23-24, 1295.

[3] M. Y. Kolawole, J. O. Aweda, S. Abdulkareem, S. A. Bello, Eur. J. Mater. Sci. Eng. **2020**, 5, 115.

[4] B. Jia, H. Yang, Z. Zhang, X. Qu, X. Jia, Q. Wu, Y. Han, Y. Zheng, K. Dai, Bioact. Mater. **2021**, 6,1588.

[5] K. Prasad, O. Bazaka, M. Chua, M. Rochford, L. Fedrick, J. Spoor, R. Symes, M. Tieppo, C. Collins, A. Cao, D. Markwell, K. Ostrikov, K. Bazaka, Materials **2017**,10, 884.

[6] J. Zhou, X. Guo, Q. Zheng, Y. Wu, F. Cui, B. Wu, Colloids Surf. B. Biointerfaces **2017**,152, 124.

[7] G. K. Levy, J. Goldman, E. Aghion, Metals **2017**, 7, 402.

[8] H. Kabir, K. Munir, C. Wen, Y. Li, Bioact. Mater. **2021**, 6, 836.

[9] D. Vojtěch, J. Kubásek, J. Čapek, I. Pospíšilová, Mater. Technol. **2015**, 49, 877.

[10] Q. Dai, S. Peng, Z. Zhang, Y. Liu, M. Fan, F. Zhao, Front. Bioeng. Biotechnol. **2021**, 9, 635338.

[11] Y. Su, I. Cockerill, Y. Wang, Y.-X. Qin, L. Chang, Y. Zheng, D. Zhu, Trends Biotechnol. **2019**, 37, 428.

[12] M. Heiden, E. Walker, L. Stanciu, J. Biotechnol. Biomater. **2015**, 5, 178.

[13] X. Xiao, E. Liu, J. Shao, S. Ge, J. Appl. Biomater. Funct. Mater. **2021**, 19, 22808000211062407.

[14] H. Yang, B. Jia, Z. Zhang, X. Qu, G. Li, W. Lin, D. Zhu, K. Dai, Y. Zheng, Nat. Commun. **2020**,11, 401.

[15] E. Mostaed, M. Sikora-Jasinska, J. W. Drelich, M. Vedani, Acta Biomater. **2018**, 71, 1.

[16] A. Kafri, S. Ovadia, J. Goldman, J. Drelich, E. Aghion, Metals **2018**, 8, 153.

[17] Z. Orsagova Kralova, R. Gorejova, R. Orinakova, M. Petrakova, A. Oriřak, M. Kupkova, M. Hrubovcakova b, T. Sopcak b, M. Balaž c, I. Maskalova d, A. Kovalcíikova, K. Koval, Prog. Nat. Sci.: Mater. Int. **2021**, 31, 279.

[18] J. Lin, X. Tong, Q. Sun, Y. Luan, D. Zhang, Z. Shi, K. Wang, J. Lin, Y. Li, M. Dargusch, C. Wen, Acta Biomater. **2020**, 115, 432.

[19] A. H. Yusop, A. A. Bakir, N. A. Shaharom, M. R. Abdul Kadir, H. Hermawan, Int. J. Biomater. **2012**, 2012, 641430.

[20] M. Bobby Kannan, C. Moore, S. Saptarshi, S. Somasundaram, M. Rahuma, A. L. Lopata, Sci. Rep. **2017**, 7, 15605.

[21] M. Krystýnová, P. Doležal, S. Fintová, M. Březina, J. Zapletal, J. Wasserbauer, Metals **2017**, 7, 396.

[22] Y. Li, P. Pavanram, J. Zhou, K. Lietaert, F. S. L. Bobbert, Y. Kubo, M. A. Leeflang, H. Jahr, A. A. Zadpoor, Biomater. Sci. **2020**, 8, 2404.

[23] B. Jia, Y. Hongtao Yang, Z. Z. Han, Q. Xinhua, Y. Zhuang, W. Qiang, Y. Zheng, K. Dai, Acta Biomater. **2020**,108, 358.

[24] T. Huang, Y. Zheng, Y. Han, Regen. Biomater. **2016**, 3, 205.

[25] Z. Tang, H. Huang, J. Niu, L. Zhang, H. Zhang, J. Pei, J. Tan, G. Yuan, Mater. Des. **2017**,117, 84.

[26] X. Shao, X. Wang, F. Xu, T. Dai, J. G. Zhou, J. Liu, K. Song, L. Tian, B. Liu, Y. Liu, Bioact. Mater. **2022**, 7, 154.

[27] Q. Yu, X. Sun, J. Zhao, L. Zhao, Y. Chen, L. Fan, Z. Li, Y. Sun, M. Wang, F. Wang, Nutr. Metab. **2019**,16, 73.

[28] J. M. Seitz, M. Durisin, J. Goldman, J. W. Drelich, Adv. Healthc. Mater. **2015**, 4, 1915.

[29] R. Oriňaková, R. Gorejová, Z. Orságová Králová, L. Haverová, A. Oriňak, I. Maskalová, M. Kupková, M. Džupon, M. Balaž, M. Hrubovčáková, T. Sopčák, A. Zubrik, M. Oriňak, Appl. Surf. Sci. **2020**, 505, 144634.

[30] L. Haverová, R. Oriňaková, A. Oriňak, R. Gorejová, M. Baláž, P. Vanýsek, M. Kupková, M. Hrubovčáková, P. Mudroň, J. Radoňák, Z. Orságová Králová, A. M. Turoňová, Metals **2018**, 8, 499.

[31] R. Oriňaková, R. Gorejová, J. Macko, A. Oriňak, M. Kupková, M. Hrubovčáková, J. Ševc, R. M. Smith, Appl. Surf. Sci. **2019**, 475, 515.

[32] R. Oriňaková, R. Gorejová, M. Petráková, Z. Orságová Králová, A. Oriňak, M. Kupková, M. Hrubovčáková, M. Podobová, M. Baláž, R. M. Smith, Materials **2020**, 13, 4134.

[33] R. Gorejová, I. Šišoláková, P. Cipa, R. Džunda, T. Sopčák, A. Oriňak, R. Oriňaková, Materials 2021,14, 4983.

[34] ASTM, Standard Guide for Laboratory Immersion Corrosion Testing of Metals, ASTM, West Conshohocken, PA 2012.

[35] ISO 8407:2009 (E), Corrosion of Metals and Alloys-Removal of Corrosion Products from Corrosion Test Specimens, International Standard ISO 8407, 2nd ed., International Standard Organisation, Geneva, Switžerland **2009**.

[36] Int. Stand. **2009**, 10993-5, 46.

[37] R. Cuscá, E. Alarcán-Llado, J. Ibaněž, L. Artús, J. Jiméněž, B. Wang, M. J. Callahan, Phys. Rev. B **2007**, 75, 165202.

[38] J. Gao, X. Zhang, Y. Sun, Q. Zhao, D. Yu, Nanotechnology **2010**, 21, 245703.

[39] C. Li, J. Lv, S. Yao, J. Hu, Z. Liang, Nucl. Inst. Methods Phys. Res. B **2013**, 295, 11.

[40] J. Maxfield, I. W. Shepherd, Polymer **1975**,16, 505.

[41] A. Vervaeck, T. Monteyne, L. Saerens, T. De Beer, J. P. Remon, C. Vervaet, Eur. J. Pharm. Biopharm. **2014**, 88,472.

[42] M. Kožielski, J. Mol. Liq. **2006**,128, 105.

[43] B. Bozzini, L. D'Uržo, C. Mele, V. Romanello, J. Mater. Sci. Mater. Electron. **2006**,17, 915.

[44] T. Miyažawa, K. Fukushima, Y. Ideguchi, J. Chem. Phys. **1962**, 37, 2764.

[45] D. Yamini, G. Devanand Venkatasubbu, J. Kumar, V. Ramakrishnan, Spectrochim. Acta A Mol. Biomol. Spectrosc. **2014**, 117, 299.

[46] Avantage software 6.5.0, XPS knowledge database. ThermoFisher Scientific, UK.

[47] S. J. Kerber, T. L. Barr, G. P. Mann, W. A. Brantley, E. Papažoglou, J. C. Mitchell, J. Mater. Eng. Perform. **1998**, 7, 329.

[48] Z.-Z. Shi, X.-X. Gao, H.-T. Chen, X.-F. Liu, A. Li, H.-J. Zhang, L.-Ň. Wang, Mater. Sci. Eng. C **2020**, 116, 111197.

[49] X. Liu, J. Sun, F. Zhou, Y. Yang, R. Chang, K. Qiu, Z. Pu, L. Li, Y. Zheng, Mater. Des. **2016**, 94, 95.

[50] H. F. Li, X. H. Xie, Y. F. Zheng, Y. Cong, F. Y. Zhou, K. J. Qiu, X. Wang, S. H. Chen, L. Huang, L. Tian, L. Qin, Sci. Rep. **2015**, 5, 10719.

[51] M. Salama, M. F. Važ, R. Colaço, C. Santos, M. Carmežim, J. Funct. Biomater. **2022**,13, 72.

[52] R. Gorejová, L. Haverová, R. Oriiňaková, A. Oriňak, M. Oriňak, J. Mater. Sci. **2019**, 54, 1913.

[53] Y. Xu, Y. Xu, W. Zhang, M. Li, H.-P. Wendel, J. Geis-Gerstorfer, P. Li, G. Wan, S. Xu, T. Hu, Front. Chem. 2022, 10, 860040.

[54] A. Kafri, S. Ovadia, G. Yosafovich-Doitch, E. Aghion, J. Mater. Sci. Mater. Med. **2018**, 29, 94.

[55] A. Sagasti, V. Palomares, J. M. Porro, I. Orúe, M. B. Sánchez-Ilárduya, A. C. Lopes, J. Gutiérrez, Materials **2019**, 13, 57.

[56] P. Li, C. Schille, E. Schweižer, F. Rupp, A. Heiss, C. Legner, U. E. Klotz, J. Geis-Gerstorfer, L. Scheideler, Int. J. Mol. Sci. **2018**, 19, 755.

[57] J. Čapek, J. Kubasek, J. Pinc, J. Fojt, S. Krajewski, F. Rupp, P. Li, Mater. Sci. Eng. C **2021**,122, 111924.

[58] Y. Qi, X. Li, Y. He, D. Zhang, J. Ding, ACS Appl. Mater. Interfaces **2019**, 11, 202.

[59] A. H. Md Yusop, N. M. Daud, H. Nur, M. R. A. Kadir, H. Hermawan, Sci. Rep. **2015**, 5, 11194.

[60] X. Liu, S. Chen, H. Ma, G. Liu, L. Shen, Appl. Surf. Sci. **2006**, 253, 814.

61] R. M. Souto, Y. González-García, A. C. Bastos, A. M. Simoes, Corros. Sci. **2007**, 49, 4568.

[62] Z. Zhen, T.-F. Xi, Y.-F. Zheng, Trans. Nonferrous Met. Soc. China **2013**, 23, 2283.

[63] J. P. Eubeler, M. Bernhard, T. P. Knepper, TrAC Trends Anal. Chem. **2010**, 29, 84.

[64] J. Ulbricht, R. Jordan, R. Luxenhofer, Biomaterials **2014**, 35, 4848.

[65] E. Guilminot, F. Dalard, C. Degrigny, Corros. Sci. **2002**, 44, 2199.

[66] S. E. Faidi, G. Jones, J. D. Scantlebury, Electrochim. Acta **1987**, 32, 947.

[67] H. Boudellioua, Y. Hamlaoui, L. Tifouti, F. Pedraza, Appl. Surf. Sci. **2019**, 473, 449.